

Preferential Nanoreinforcement of Thermoplastic Polyurethane Elastomers with Dispersed Nano-Clay

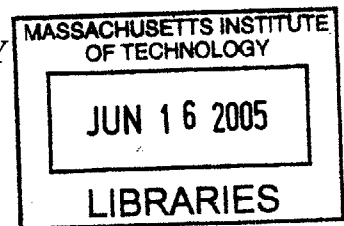
by

Shawna M. Liff
B.S. in Mechanical Engineering
Northeastern University, 2003

SUBMITTED TO THE DEPARTMENT OF MECHANICAL ENGINEERING IN PARTIAL
FULFILLMENT OF THE REQUIREMENTS FOR THE DEGREE OF

MASTER OF SCIENCE IN MECHANICAL ENGINEERING
AT THE
MASSACHUSETTS INSTITUTE OF TECHNOLOGY

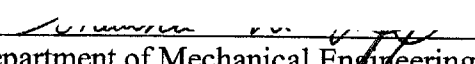
JUNE 2005



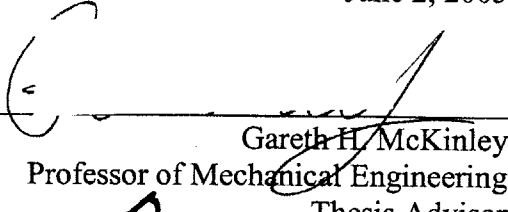
© 2005 Shawna M. Liff. All rights reserved.

The author hereby grants to MIT permission to reproduce and to distribute publicly paper and electronic copies of this theses document in whole or in part.

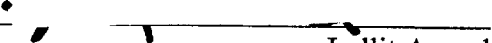
Signature of Author


Department of Mechanical Engineering
June 2, 2005

Certified by


Gareth H. McKinley
Professor of Mechanical Engineering
Thesis Advisor

Accepted by


Lallit Anand
Professor of Mechanical Engineering
Chair, Committee on Graduate Students

ARCHIVES



Room 14-0551
77 Massachusetts Avenue
Cambridge, MA 02139
Ph: 617.253.2800
Email: docs@mit.edu
<http://libraries.mit.edu/docs>

DISCLAIMER OF QUALITY

Pagination issues by author, all content is accounted for.

Preferential Nanoreinforcement of Thermoplastic Polyurethane Elastomers with Dispersed Nano-Clay

by

Shawna M. Liff

Submitted to the Department of Mechanical Engineering
on June 2, 2005 in partial fulfillment of the
requirements for the Degree of
Master of Science in Mechanical Engineering

Abstract

It is difficult for scientists to engineer elastomeric materials that are both strong and tough like spider dragline silk. Inspired by the morphology of spider dragline silk and motivated to develop strong, tough, elastomeric polyurethanes to be used in soldier applications I have prepared polyurethane/clay nanocomposites. Polymer/clay nanocomposites have exhibited great potential for providing enhanced and possibly-tunable thermomechanical behavior. However, the biggest challenge facing advances in polymer/clay nanocomposites is the complete dispersion of nano-clay within the polymer matrix due to thermodynamic and kinetic limitations. A novel solvent exchange method to fully exfoliate and disperse discotic smectic clay, Laponite (diameter = 25 nm, thickness = 1 nm), in three thermoplastic polyurethane elastomers (TPUs)—Elasthane 80A, HDI-PTMO PU, and PU-1-33—has been developed. This clay was selected because the diameter of one platelet is similar to the lateral dimension of a single hard-domain in block-polymeric TPU. WAXD, TEM, and AFM phase imaging of cast films following solvent exchange show that the nano-clay is well dispersed in the TPUs. Uniaxial mechanical testing showed that as much as a 23-fold increase in elastic modulus, 100% increase in toughness, and 50% increase in strength can be achieved without a reduction in extensibility when Laponite is added to Elasthane. Furthermore, the heat distortion temperature of the Elasthane can be increased from 101°C to more than 200°C, as measured by DMA, when 20 wt% Laponite is added. The HDI-PTMO PU/Laponite nanocomposites behave like the Elasthane/Laponite nanocomposites, exhibiting an increase in elastic modulus, strength, and toughness without a loss in extensibility. In contrast, a PU-1-33 thin film exhibits a significant decrease in extensibility, strength, and toughness with no significant change in elastic modulus when filled with Laponite. Characterization shows that the Laponite is preferentially embedded within the polar hard domains of the Elasthane and HDI-PTMO PU and embedded within the soft domain of PU-1-33. The Laponite is attracted to the polar, hydrophilic soft segment constituent, polyethylene oxide, in PU-1-33. Ultimately, Laponite can be used to strengthen and toughen TPUs and the location of Laponite reinforcement can be altered by adjusting the polarity and hydrophilicity of the soft segment.

Thesis Advisor: Gareth H. McKinley
Title: Professor of Mechanical Engineering

Acknowledgements

This research was supported by the US Army through the Institute for Soldier Nanotechnologies, under Contract DAAD-19-02-D-0002 with the US Army Research Office. The content does not necessarily reflect the position of the Government, and no official endorsement should be inferred.

I also want to thank the National Science Foundation for the financial support it provided in the form of a graduate research fellowship.

Furthermore, I would like to thank Professor Gareth H. McKinley, my advisor, for sharing his expertise and offering support and guidance. I am also grateful for the friendship, mentorship, and open-mindedness Dr. Nitin Kumar and Dr. LaShanda James-Korley afforded me. Their support and knowledge was invaluable.

I also want to thank my lab-mates at the Institute for Soldier Nanotechnologies and at the Non-Newtonian Fluids Laboratory for their help. I want to thank Dr. Sabine Cantournet, a visiting professor from France, for her help with the polyurethane modeling. I also want to thank the Center for Material Science and Engineering Staff, specifically Tim McClure, Joseph A. Adario, Michael Frongillo and Patrick Boisvert, who taught me to use the characterization equipment in their respective labs.

I would also like to wholeheartedly acknowledge and thank my family and friends for their continuing support, patience, and love.

Table of Contents

List of Figures	6
List of Tables	9
1. Introduction.....	10
2. Background and Motivation	25
2.1 Spider Silk.....	25
2.2 Thermoplastic Polyurethane	27
2.3 Polymer-Clay Nanocomposites	29
3. Polyurethane/Clay Nanocomposite Literature Review.....	32
3.1 Detailed Synopsis of Previous Findings	32
3.2 Summary	41
4. Experimental Procedures	42
4.1 Polyurethane Nanocomposite Preparation.....	42
4.1.1 Materials Utilized.....	42
4.1.1.1 Laponite	42
4.1.1.2 Elasthan 80A	43
4.1.1.3 PU-1-33.....	43
4.1.1.4 HDI-PTMO PU	44
4.1.2 Solvent Exchange Approach to Fully Disperse Nanoparticles	44
4.1.3 Preparation of Thin-film Nanocomposites.....	46
4.2 Characterization Methods	47
4.2.1 Transmission Electron Microscopy	48
4.2.1.1 Operating Concept	48
4.2.1.2 Test Procedure	48
4.2.2 Atomic Force Microscopy	49
4.2.2.1 Operating Concept	49
4.2.2.2 Test Procedure	50
4.2.3 Wide Angle X-Ray Diffraction.....	51
4.2.3.1 Operating Concept	51
4.2.3.2 Test Procedure	52
4.2.4 Thermogravimetric Analysis	52
4.2.4.1 Operating Concept	52
4.2.4.2 Test Procedure	53
4.2.5 Differential Scanning Calorimetry.....	53
4.2.5.1 Operating Concept	53
4.2.5.2 Test Procedure	55
4.2.6 Dynamic Mechanical Analysis	55
4.2.6.1 Operating Concept	56

4.2.6.2 Test Procedure	56
4.2.6.3 Static Thermomechanical Analysis.....	57
4.2.7 Zwick Mechanical Testing.....	57
4.2.7.1 Operating Concept	57
4.2.7.2 Test Procedure	58
4.2.8 Optical Microscopy Using Cross-Polarized Light.....	59
4.2.8.1 Operating Concept	59
4.2.8.2 Test Procedure	60
4.3 Summary	61
5. Results and Discussion	62
5.1 Evidence of Exfoliation	62
5.2 Mechanical Enhancement	64
5.3 Thermomechanical Enhancement.....	67
5.4 Thermal Behavior	69
5.5 Evidence of Long Range Ordering	73
5.6 Thermal Degradation	75
5.7 Novel Polyurethane/Laponite Nanocomposites Characterization Results	76
5.7.1 Evidence of Exfoliation	76
5.7.2 Mechanical Enhancement	78
5.7.3 Thermomechanical Enhancement.....	79
5.7.4 Thermal Behavior	80
5.7.5 Evidence of Long Range Order	81
6. Conclusions.....	83
7. Future Work	86
7.1 Laponite Movement during Deformation	86
7.2 Influence of Laponite on Hydrogen and Ionic Bonding.....	91
7.3 Influence of Laponite at Various Temperatures	91
7.4 Influence of Thermal Treatments on Nanocomposite Mechanical Behavior	91
7.5 Summary	93
References.....	94
Appendix A: Tabulated Synopsis of Previous Polyurethane/Clay Literature	100
Appendix B: ABAQUS Input File.....	107
Appendix C: ABAQUS Subroutine File.....	109

List of Figures

Figure 2.1:	Engineering stress-strain curves of dragline and viscid silk as displayed in [2].....	25
Figure 2.2:	A urethane linkage.....	27
Figure 2.3:	Thermomechanical behavior of various polyurethanes.....	28
Figure 2.4:	Schematic illustrations of various polymer-clay nanocomposites with different extents of clay dispersal.....	30
Figure 2.5:	Comparison of the Montmorillonite and Laponite crystal structure as shown in [31].....	31
Figure 3.1:	Tensile properties of the polyurethane-clay nanocomposites prepared with the longest onium ion Montmorillonite-modification at various clay loadings as reported in [32]: (A) tensile strength, (B) tensile modulus, and (C) strain-at-break.....	32
Figure 3.2:	Dispersal of 1 wt% Montmorillonite modified with most reactive swelling agent in the PU containing 39 wt% hard segment as shown in [38].....	34
Figure 3.3:	Representative force-extension curves of the polyurethane urea nanocomposites in [40].....	34
Figure 3.4:	Storage moduli(left) and stress-strain plots (right) of the polyurethane containing 0 (a), 4 (b), 20 (c), and 40 (d) wt% clay from [42].....	35
Figure 3.5:	Transmission Electron Micrographs of the solvent cast (left) and melt compounded (right) soft polyurethane nanocomposites containing 3 wt% Montmorillonite depicted in [46].....	36
Figure 3.6:	Storage modulus versus strain amplitude curves of the polyethylene-polyurethane (PEPU) nanocomposites containing 0, 2.5, and 5 wt% clay depicted in [47].....	37
Figure 3.7:	Evolution of <i>d</i> -spacing with respect to a nanocomposite loaded with 5 wt% clay during stretching.....	38
Figure 3.8:	Tapping mode AFM phase images of (a) pure polyurethane containing 36 wt% hard segment and (b) the same polyurethane loaded with 1 wt% clay in [24]. The small spherical aggregates are hard domains and the large masses shown in (b) are clay tactoids.....	39
Figure 3.9:	Mechanical properties of the waterborne PU filled with various weight concentrations of Saponite as shown in [60].....	40
Figure 4.1:	Idealized unit cell of Laponite from [11]... ..	42
Figure 4.2:	Structure of Elasthane 80A based on available non-proprietary information.....	43
Figure 4.3:	Structure of PU-1-33 [65].....	43
Figure 4.4:	Structure of HDI-PTMO PU [66].....	44
Figure 4.5:	Vapor-Liquid equilibrium curve for H ₂ O and for DMAc.....	45
Figure 4.6:	Vapor-Liquid equilibria of H ₂ O-DMAc determined via experiment in [68].....	45
Figure 4.7:	Photograph of the Teflon block filled with red dye to elucidate the internal dimensions.....	47
Figure 4.8:	Photograph of a thin-film polyurethane/Laponite nanocomposite removed from the Teflon plate after drying.....	47
Figure 4.9:	Photograph of the nanocomposite thin-film fixed with epoxy upon a cryotome post.....	49

Figure 4.10: Photograph of the pig eyelash used to place the cryotomed sample on the carbon mesh.....	49
Figure 4.11: AFM operating regions displayed on an interatomic force versus distance curve as presented in [72].....	50
Figure 4.12: Diffraction image describing the derivation of Bragg's Law.....	52
Figure 4.13: Heat flux DSC schematic as shown in [75].....	54
Figure 4.14: Heat distortion comparison of pure Elasthane and 20 wt% Laponite-filled Elasthane experimental set-up.....	57
Figure 4.15: Heat distortion comparison set-up zoomed view (pure Elasthane—left, 20 wt% Laponite-filled Elasthane—right).....	57
Figure 4.16: Demonstrative engineering stress-strain curve and depiction of the mechanical properties calculated.....	58
Figure 4.17: Photograph of the Zwick/Roell thin film grips.....	59
Figure 4.18: Image depicting the path light travels through cross-polarized filters.....	60
Figure 5.1: Wide angle x-ray diffraction spectra for pure Elasthane, 10 wt% Laponite in Elasthane, 20 wt% Laponite in Elasthane, and pure Laponite.....	62
Figure 5.2: TEM image of 10 wt% Laponite (dark lines) in Elasthane where the image width is equal to 118 nm.....	63
Figure 5.3: AFM phase image of 10 wt% Laponite (bright fields) in Elasthane where the image width is equal to 374 nm.....	63
Figure 5.4: Representative tensile curves of Elasthane/Laponite nanocomposites at various Laponite loadings.....	64
Figure 5.5: Zoomed view of representative tensile curves of the nanocomposites between 0 and 100% elongation.....	64
Figure 5.6: Young's modulus of nanocomposites at various Laponite loadings and predictions: Guth-Gold rigid particle filler prediction—solid red line and best fit power-law scaling—dashed blue line.....	65
Figure 5.7: Toughness of nanocomposites at various Laponite loadings. Toughness based on material stretched to failure (black squares) and stretched to 30% engineering strain (red circles).....	65
Figure 5.8: Ultimate strength (black circles) and extensibility (red triangles) of nanocomposites at various Laponite loadings.....	65
Figure 5.9: Comparison of stiffness and toughness of various materials.....	66
Figure 5.10: Comparison of strength and toughness of various materials.....	66
Figure 5.11: Flexural storage moduli of nanocomposites at various Laponite loadings.....	67
Figure 5.12: Loss tangent of nanocomposites at various Laponite loadings.....	67
Figure 5.13: Comparison of elastic modulus to flexural storage modulus at 25°C of the nanocomposites at various weight fractions of Laponite.....	68
Figure 5.14: Comparison of pure and 20 wt% Laponite-filled Elasthane after dynamic mechanical analysis.....	69
Figure 5.15: Comparison of heat distortion behavior of pure and 20 wt% Laponite-filled Elasthane at 40°C and 90°C.....	69
Figure 5.16: Compliance of pure and 20 wt% Laponite-filled Elasthane.....	69
Figure 5.17: First cycle of the DSC heat flow for the various nanocomposite.....	70
Figure 5.18: Second cycle of the DSC heat flow for the various nanocomposites.....	70

Figure 5.19: Comparison of the DSC heat flow for pure and 10 wt% Laponite-filled polytetramethylene oxide.....	71
Figure 5.20: DSC heat flow for pure Laponite powder.....	71
Figure 5.21: Modulated DSC heat flow of the various nanocomposites.....	73
Figure 5.22: Modulated DSC non-reversible heat flow of the various nanocomposites.....	73
Figure 5.23: Cross-polarized image of the grip locale of nanocomposite containing 10 wt% Laponite after a tensile test. Dark field corresponds to the un-stretched amorphous region, pink field corresponds to strain induced ordering.....	74
Figure 5.24: Zoomed cross-polarized view of a crystallite within the amorphous un-stretched region of a nanocomposite containing 10 wt% Laponite.....	74
Figure 5.25: Melting of crystallites within the Elasthane/Laponite nanocomposite containing 10 wt% Laponite.....	75
Figure 5.26: Re-crystallization of the crystallites within the Elasthane/Laponite nanocomposite containing 10 wt% Laponite, upon annealing at 60°C.....	75
Figure 5.27: Degradation behavior of various Elasthane/Laponite nanocomposites as temperature increases.....	76
Figure 5.28: Degradation temperature and residue fraction behavior of the nanocomposites with respect to Laponite concentration.....	76
Figure 5.29: TEM image of 10 wt% Laponite (dark lines) in PU-1-33 where the width of the image is 368 nm.....	77
Figure 5.30: TEM image of 10 wt% Laponite (dark lines) in HDI-PTMO PU where the width of the image is 368 nm.....	77
Figure 5.31: WAXD spectra of HDI:BDO hard segment, PU-1-33, PU-1-33 with 10 wt% Laponite, and Laponite (listed from bottom).....	77
Figure 5.32: WAXD spectra of HDI:BDO hard segment, HDI-PTMO PU, HDI-PTMO PU with 10 wt% Laponite, and Laponite (listed from bottom).....	77
Figure 5.33: Tensile curve comparison of the various pure polyurethanes (b, c, f) and their corresponding nanocomposite filled with 10 wt% Laponite (a, d, e).....	78
Figure 5.34: Flexural storage modulus of the pure PU-1-33 and HDI-PTMO PU (black) and their respective nanocomposites containing 10 wt% Laponite (red).....	80
Figure 5.35: Loss tangent of the pure PU-1-33 and HDI-PTMO PU (black) and their respective nanocomposites containing 10 wt% Laponite (red).....	80
Figure 5.36: First cycle of DSC heat flow of the pure PU-1-33 and HDI-PTMO PU and their respective nanocomposites filled with 10 wt% Laponite.....	81
Figure 5.37: Second cycle of DSC heat flow of the pure PU-1-33 and HDI-PTMO PU and their respective nanocomposites filled with 10 wt% Laponite.....	81
Figure 5.38: Cross-polarized microscopic image of pure HDI-PTMO PU.....	82
Figure 5.39: Cross-polarized microscopic image of the HDI-PTMO PU filled with 10 wt% Laponite.....	82
Figure 5.40: Cross-polarized microscopic image of pure PU-1-33.....	82
Figure 5.41: Cross-polarized microscopic image of PU-1-33 filled with 10 wt% Laponite.....	82
Figure 6.1: Cartoon displaying the preferential location of Laponite in the various polyurethane nanocomposites investigated.....	85
Figure 7.1: Qi & Boyce thermoplastic polyurethane stress-strain constitutive model and parameters presented in [85].....	88
Figure 7.2: Model 4 fit (cyan) to pure Elasthane data (black).....	89

Figure 7.3:	Influence of adjustments in model parameters on stress-strain curve.....	90
Figure 7.4:	Hysteretic behavior of pure Elasthane (black), 10 wt% (red), and 20 wt% (green) Laponite-filled Elasthane.....	90

List of Tables

Table 2.1:	Comparison of the mechanical properties of silk to other high-performance materials [2].....	26
Table 3.1:	The molecular weight, tensile strength, elongation, and water absorption of the pure polyurethane and polyurethane-Montmorillonite nanocomposites prepared in [36].....	33
Table 3.2:	List and comparison of the various clays investigated for polyurethane reinforcement [25, 55-57].....	40
Table 5.1:	Heat Distortion Temperature (HDT) of the nanocomposites at various weight concentrations of Laponite.....	68
Table 5.2:	Mechanical Properties of pure HDI-PTMO PU and its nanocomposite containing 10 wt% Laponite.....	79
Table 5.3:	Mechanical Properties of pure PU-1-33 and its nanocomposite containing 10 wt% Laponite.....	79
Table 6.1:	Polyurethane soft segment polarity expressed in terms of the solubility parameter which was calculated using the group contribution method and values given in [78].....	84
Table 7.1:	Parameters used in Model 4 to predict the behavior of pure Elasthane.....	89
Table 7.2:	Corresponding parameter values for the various models depicted in Figure 7.3.....	90

1. Introduction

For years scientists have marveled at the exceptional combination of strength and toughness spider silk fibers exhibit. An orb-web-weaving araneid spider can produce a family of silk fibers, each with a specific function [1]. The stiffest, least extensible fiber, dragline silk, holds the weight of the spider as it drops from one tree limb to the next and forms the frame of the web, while a more extensible fiber, viscid silk, forms the secondary, fly-trapping spirals of the web [2]. Despite the differences in stiffness and extensibility, each of these high strength fibers exhibits approximately the same magnitude of toughness, making spider silk fibers a superior energy absorbing material.

Materials that exhibit superior energy absorbency, high strength, and some extensibility are desirable in numerous applications, including in protective active apparel and in product packaging. However, unlike spiders, engineers have difficulty manufacturing materials that are both strong and tough. Thomas Hahn, a mechanical and aerospace engineering professor at the University of California, Los Angeles has remarked, “Normally we [engineers] can make material very strong, but at the expense of toughness and we can make things very tough but at the expense of strength. Combining the two characteristics—as the spider does—is our challenge” [3]. Consequently, since spider silk cannot yet be harvested or produced on a feasible mass scale, polymeric analogs or polymeric nanocomposites offer a possible route for the development of high energy-absorbing, silk-like materials [1, 4, 5].

At the Institute for Soldier Nanotechnologies, I am working with a team of researchers to develop energy absorbing materials to be used in soldier uniforms. These materials must exhibit tremendous toughness and good resistance to wear, tear, cut and puncture, but maintain moderate strength and flexibility. Therefore, aware of the nanostructure from which the exceptional mechanical properties of spider dragline silk are derived, I chose to develop polyurethane/clay nanocomposites and investigate their resultant energy absorbency capabilities. Thermoplastic polyurethane was chosen as the matrix polymer because like spider silk it is a semi-crystalline, block-polymeric, elastomeric material that exhibits good extensibility and stiffness. The stiffness of thermoplastic polyurethanes and the weaker, viscid, spider silks are similar in magnitude. Unfortunately, the strength exhibited by polyurethanes is inferior to the strength displayed by spider silks [6]. So, inspired by the efficacy of clay to inexpensively strengthen polymers I chose to reinforce the thermoplastic polyurethane with nano-clay [7].

Nano-clay, an inorganic substance with a large surface-area-to-volume ratio, is an affordable nano-filler that can dramatically enhance the mechanical and barrier properties and heat resistance of polymer matrices without significantly increasing the weight of the material [8, 9]. In the late 1980s Toyota Research Labs first proved the efficacy of clay to nanoreinforce polymers. By adding less than 5 wt% clay to nylon, researchers were able to significantly enhance the mechanical properties, heat resistance, and dimensional stability of the nylon and utilize the material in an under-the-hood automotive application, i.e. as a timing belt cover [7]. Motivated by other automotive, food packaging, and construction applications, numerous research groups have investigated other polymer/clay nanocomposite systems and have provided evidence that nano-clay can effectively reinforce polymer matrices [8, 9].

Clay nanoreinforcement could potentially be used to develop polymer-based families of high-performance materials with enhanced and possibly tailored mechanical, thermal, and barrier properties. However, the key to developing high-performance polymer/clay nanocomposites is fully dispersing and exfoliating inorganic, hydrophilic clay within organic and often hydrophobic polymer matrices. If the clay is not well dispersed, the clay aggregates and behaves as micro-scale filler rather than as nano-scale reinforcement and the resultant material acts as a conventional composite, displaying poor strength and toughness [8]. To enhance dispersal and avoid aggregation, Dr. Nitin Kumar and I developed a novel solvent exchange approach to exfoliate nanoparticles [10]. The nano-clay utilized, Laponite RD, was fully dispersed in the thermoplastic polyurethanes using this novel solvent exchange approach.

Laponite, a commercial, synthetic smectic clay with monodisperse platelets measuring 25 nm in diameter and 0.92 nm in thickness was chosen because of its size [11]. Because spiders modify the silk stiffness and strength by regulating polypeptide chain ordering and/or crystalline structure formation during spinning, it was important that I modified the stiffness of the polyurethane by adding and dispersing clay that shared the same lateral scale as the hard crystalline domains within the polyurethane [5, 12]. The nanoreinforcement capabilities of Laponite were evaluated in three polyurethanes, including Elasthane 80A, a commercial polyurethane, and two novel polyurethanes HDI-PTMO PU and PU-1-33.

The following paper details the inspiration for, preparation of, and characterization of three different polyurethane/clay nanocomposites. The resultant thermomechanical properties of the Elasthane-based nanocomposite are emphasized. In Chapter 2, I detail the findings of previous researchers that inspired my development of polyurethane-Laponite nanocomposites as synthetic, high-energy-absorbency materials. In Chapter 3 I briefly review the work of others who have developed polyurethane-clay nanocomposites. In Chapter 4 I discuss how my polyurethane-Laponite nanocomposites were prepared, specifically, how the Laponite was fully-dispersed throughout the polyurethanes, and how the resultant nanocomposites were characterized. Furthermore, in Chapter 5 I report and discuss the results of the polyurethane/clay nanocomposite characterization which showed the Laponite was well dispersed and the resultant thermomechanical properties of the Elasthane were significantly enhanced. Finally, in Chapter 6 I summarize the unique properties and high-performance behavior of the three polyurethane-Laponite nanocomposites and in Chapter 7 I discuss the future investigations involving these nanocomposites that will be pursued.

2. Background and Motivation

The following sections provide more detailed information regarding the findings of previous researchers, which inspired the development of the thermoplastic polyurethane-Laponite nanocomposites as synthetic, high-energy-absorbency materials. The structural, mechanical, and thermal properties of spider silk and thermoplastic polyurethanes are examined and compared. Furthermore, the efficacy of clay nanoreinforcement in polymers is evidenced and the major challenge facing the development of polymer-clay nanocomposites is discussed.

2.1 Spider Silk

Spider silk is nature's high-performance polymer. The orb-web-weaving araneid spider can produce a family of high-performance silk fibers that exhibit superior energy absorbency capabilities in conjunction with various combinations of extensibility, stiffness, and strength. Each fiber in the family has a different function, depending on the mechanical properties of the fiber. These mechanical properties in turn depend upon the protein combinations excreted by the spider. Consequently, a spider is a technologically advanced fiber manufacturer, producing fibers for various functions by manipulating amino acid sequences, water content, and spinning speeds [1].

The orb-web-weaving araneid spiders are most studied because these spiders have seven glands which produce different proteins that each has a specific function [1]. For example, the major ampullate gland produces the dragline or web, frame silk and the flagelliform glands produce the core of the spiraling, fly-catching, viscid silk [1]. These fibers have completely different mechanical functions and behaviors, yet have similar energy absorbency capabilities as shown in Figure 2.1 and Table 2.1.

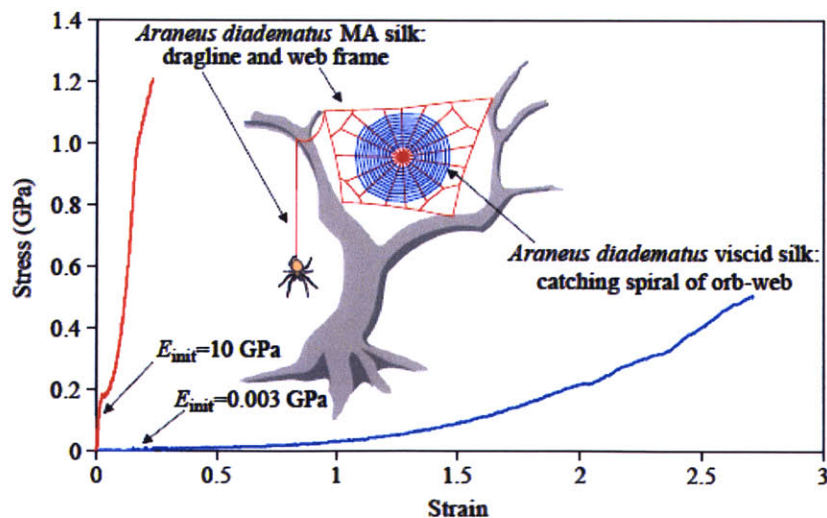


Figure 2. 1: Engineering stress-strain curves of dragline and viscid silk as displayed in [2].

The dragline silk, which must hold the weight of the spider and form the frame of the web exhibits an initial modulus of 10 GPa, an ultimate strength of 1.1 GPa, a 27% extensibility and a toughness of 160 MJ m⁻³ [2]. The viscid silk, which must bend extensively to slow and trap flies that collide with the web, exhibits a similar toughness of 150 MJ m⁻³, but instead an initial modulus of 3 MPa, a 270% extensibility, and an ultimate strength of 500 MPa [2]. Other natural and synthetic materials may exhibit similar combinations of stiffness, extensibility and strength to silk, but the toughness of native-spider silk is unmatched as is shown in Table 2.1. Synthetic rubber comes closest to matching the toughness of the weaker, viscid silk, but the ultimate strength exhibited by the viscid silk is unachievable in synthetic or natural rubbers. Consequently, knowledge of the amino acid sequence and morphology of spider silk, and their relation to the mechanical properties is critical for the development of new high-performance materials.

Material	Initial Modulus [GPa]	Ultimate Strength [GPa]	Extensibility	Toughness [MJm ⁻³]
Dragline Silk	10	1.1	0.27	160
Viscid Silk	0.003	0.5	2.7	150
Synthetic Rubber	0.001	0.05	8.5	100
Nylon Fiber	5	0.95	0.18	80
Silkworm Silk	7	0.6	0.18	70
Wool	0.5	0.2	0.5	60
Kevlar 49 Fiber	130	3.6	0.027	50
Elasthane	0.038	0.032	3.9	48
Carbon Fiber	300	4	0.013	25
Tendon Collagen	1.5	0.15	0.12	7.5
High-Tensile Steel	200	1.5	0.008	6
Bone	20	0.16	0.03	4

Table 2. 1: Comparison of the mechanical properties of silk to other high-performance materials [2].

Investigation of the amino acid sequence and structural motif of the various spider silks has shown that dragline spider silk, in particular, is an optimized block copolymer. The silk is based on two proteins, spidroin I and spidroin II, sequenced by Xu and Lewis in 1990 [13]. Like multi-block polymeric systems, the resultant silk consists of hydrophilic, soft glycine-rich blocks and hydrophobic, alanine-rich hard blocks. The alanine-rich blocks hydrogen bond with each other and form small crystalline β -sheets that comprise 12% of the fiber by volume and measure approximately 2 x 5 x 7 nm³ [14]. These highly oriented β -sheets are coupled to the amorphous glycine-rich soft blocks via the less oriented β -sheets. Consequently during deformation these crystalline sheets are moved and aligned by the soft glycine-rich matrix [15]. The soft blocks give the fiber its elasticity and their structural motif is not easily identified and may consist of a combination of 3₁-helices, β -spirals, and random coils, which are probably highly ordered and hydrogen bonded [16-18]. Furthermore, the soft blocks may change conformation depending on extension and water content, providing a means for the silk to obtain the superior ultimate strength it exhibits prior to failure [17].

Dragline silk also exhibits remarkable thermomechanical behavior. At ~200°C, dynamic mechanical analysis shows that the flexural storage modulus of dragline silk drops from ~10 GPa

to ~ 2 GPa when the intermolecular hydrogen bonds of the non-crystalline domains break down [18]. This behavior is analogous to the soft segment glass transition in block-co-polymers. This material exhibits amazing heat resistance, only undergoing mechanical failure at 371°C the point when the β -crystallites break down [18]. This observed behavior is analogous to block-polymeric hard segment melting. Not only, is spider silk, dragline silk specifically, remarkable at room temperature, but the static mechanical properties between -60°C and 150°C are superior when compared to other properties [18]. Although the mechanical properties of spider silk, like polymers, are time and temperature dependent, spider silk is functional over a wider temperature range.

Spider dragline silk is a highly evolved and optimized protein polymer that has a combination of thermomechanical properties that are unmatched by synthetic materials. The strength, toughness, and heat resistance exhibited by dragline silk fibers are desirable. If these fibers could be replicated on a mass scale the potential applications are vast. At this point synthetic analogs of spider silk, like nylons, rubbers, and polyurethanes are still thermomechanically inferior to native-spider silk.

2.2 Thermoplastic Polyurethane

Polyurethanes are well-studied versatile polymers that have been used in a variety of applications, including in chair cushions, bra padding, artificial organs and other biomedical applications, in active wear (spandex/lycra), footwear, roller ski and skate wheels, ski boots, wake boards, and in paints and coatings [19, 20]. Any polymer that contains urethane linkages, depicted in Figure 2.2, is considered a polyurethane.

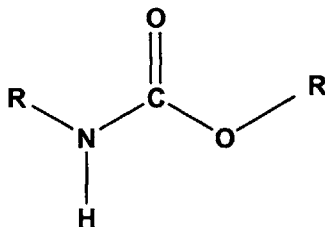


Figure 2. 2: A urethane linkage

Polyurethanes or polyurethane ureas are made by reacting diisocyanates with dialcohols or diamines, respectively [21]. The urethane linkages like to hydrogen bond and can form rigid, crystalline aggregates. In numerous applications segmented polyurethanes are desired and polyols, polymeric compounds containing alcoholic hydroxyl groups, of various lengths ($M_w \sim 600\text{-}3000 \text{ g mol}^{-1}$) are polymerized with the urethane reactants in either a one-step or two-step reaction [22]. The material properties of the segmented polyurethane can be tuned between that of a hard plastic and a flexible elastomer depending on the polyol added and the resultant chemical or physical crosslinks formed [22].

Thermoplastic polyurethanes are those segmented, elastomeric polyurethanes that contain soft polymeric segments that have a glass transition temperature (T_g) below room temperature [23]. Consequently, at temperatures below the soft segment T_g a thermoplastic polyurethane behaves as a glass, while at temperatures above the T_g the polyurethane behaves as an elastomer. The soft

segment imparts good extensibility and the rigid hydrogen bonded crystal aggregates, identified as hard domains, act as physical crosslinks imparting moderate stiffness and strength [19].

The stiffness, strength, extensibility, and thermomechanical behavior of segmented polyurethanes are dependent upon numerous factors, including the extent of phase separation between the hard and soft segment, the concentration of hard segment to soft segment, the type of polyol added, the molecular weight of the polymer, and the extent of the polymer crystallinity [22].

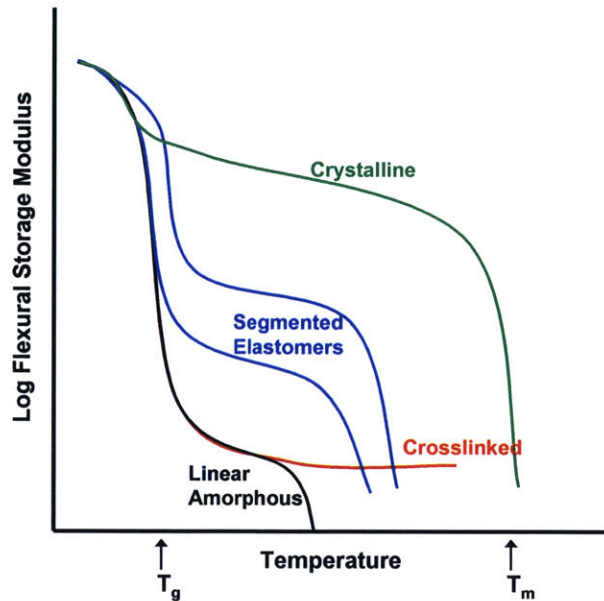


Figure 2.3: Thermomechanical behavior of various polyurethanes.

For example, soft segment crystallinity or hard segment content can be increased in segmented polyurethanes to increase the magnitude of the rubbery plateau modulus, as shown in Figure 2.3. Furthermore, an increase in polyurethane molecular weight can increase the hard segment melting temperature (T_m) or point of liquid flow without influencing the magnitude of the rubbery plateau modulus [22]. Consequently, there are numerous ways in which the thermomechanical properties of polyurethanes can be tailored.

The semi-crystalline, block-polymeric structure of elastomeric polyurethane is similar to spider silk. Each contains crystalline aggregates that act as physical crosslinks, however, the aggregates or hard domains in polyurethane, which have a lateral dimension measuring 12-32 nm in length, are bigger than the β -sheets in spider silk [24]. Furthermore, the thermomechanical properties of both materials are easily tailored. Unfortunately, the properties of thermoplastic polyurethanes are inferior to spider silk. Because the onset of the urethane dissociation is near 200°C, polyurethanes undergo a three-orders-of-magnitude change in flexural storage modulus between -100°C and 250°C while spider dragline silk undergoes less than an order-of-magnitude change within this temperature range because the dissociation of the β -sheets is well above 200°C [18, 22]. Consequently, polyurethane-based materials have the potential to be spider silk analogs if the mechanical properties and thermal stability of the polyurethane can be significantly enhanced.

2.3 Polymer-Clay Nanocomposites

Nano-clay has proven to be effective polymer filler, enhancing mechanical properties, thermal stability, and decreasing permeability of numerous polymers at small volume fractions. For example, in the late 1980s Toyota Research Labs developed a Nylon 6-Montmorillonite nanocomposite that at only a 4.2 wt% clay loading exhibited a 100% increase in initial modulus, a 50% increase in ultimate strength, and a 80°C increase in heat distortion temperature [8]. This thermomechanical enhancement was greater than that produced by glass or talc at over 30 wt% loading [7]. This finding initiated numerous investigations of other polymer-clay nanocomposites.

Nylon was not the only polymer that exhibited thermomechanical enhancements and improved barrier properties when filled with clay. The inclusion of well-dispersed clay has exhibited enhancements in a handful of other polymer systems as is shown in the list below.

- In 1993, Yano and colleagues from Toyota Research Labs in Japan found that when polyimide was filled with 2 wt% synthetic mica the water vapor permeability coefficient was less than 10% that of the pure polyimide permeability coefficient. Furthermore the thermal expansion coefficient of the composite was 60% of the pure polyimide coefficient [25].
- In 1994, Lan and Pinnavai found that when rubbery epoxy was filled with exfoliated Montmorillonite at 15 wt%, the composite exhibited more than a 10-fold increase in both tensile strength and modulus when compared to the properties of the pure epoxy [26].
- In 2001, Nam and colleagues reported that a 6 wt% loading of modified Montmorillonite in polypropylene foam resulted in a 44°C increase in heat distortion temperature when compared to the properties of the pure polypropylene [9].
- In 2002, Lepoittevin and colleagues reported that poly(ϵ -caprolactone) exhibited a higher thermal stability when filled with modified Montmorillonite. Whether the clay was exfoliated or intercalated the degradation temperature at 50% mass loss was at least 25°C higher than the degradation temperature of the pure poly(ϵ -caprolactone) at the same mass loss percentage [9].

In the past fifteen years numerous researchers have shown that clay can effectively reinforce polymer systems and significantly improve the mechanical, thermal, and barrier properties of the pure material. Consequently, reinforcing polyurethanes with clay appears to be a feasible method to enhance the thermomechanical properties of polyurethane and develop synthetic spider silk analogs.

The major challenge in developing polymer/clay nanocomposites is fully dispersing and exfoliating inorganic, hydrophilic clay platelets within organic and often hydrophobic polymer matrices. Numerous clays, including Montmorillonite, Hectorite, and Saponite among others, have been investigated as polymer filler. Whether natural or synthetic, these silicates contain alkali and alkaline earth cations absorbed on the negatively charged silicate faces which act as glue binding the silicates in stacks [9]. If the silicates and polymer matrix do not interact and the silicates remain aggregated in stacks, the mechanical properties of the material are poor [27]. However, if the silicate and polymer interact favorably the silicate stacks can be delaminated and the small-volume, high aspect-ratio, stiff platelets can offer a large surface on to which the soft polymer can transfer stress and can provide a torturous path in which permeants must traverse

Ultimately, any clay can be as effective a reinforcing agent as Montmorillonite, if the appropriate swelling agent or ammonium salt is utilized for ion exchange and the silicates are well-dispersed.

3.2 Summary

Over the past seven years researchers have investigated numerous polyurethane systems, clay fillers, chemical modifiers of clay, dispersal techniques, and nanocomposite synthesis procedures. In general the previous research suggests that the addition of clay most effectively stiffens soft polyurethanes rather than hard polyurethanes. This is because the hard domains and soft segment crystallinity are responsible for polyurethane stiffness and when clay is added to a soft polyurethane the rigidity of the polymer is enhanced, but when added to a hard polyurethane the previously established hard domain network is disrupted and the rigidity compromised [22]. The resultant strength and extensibility of a polyurethane nanocomposite increases when the clay is well dispersed and the clay, the chemical modification, and the polyurethane all interact favorably. However, if the clay induces crystallinity in the soft segment the strength and extensibility are degraded [34, 35, 42]. Furthermore, the water vapor permeability of the nanocomposites decreases with increasing clay concentration and better clay dispersal [40, 43]. The oxygen permeability, however, decreases only if the polyurethane adheres to the clay platelets [43]. These investigations show that typically the soft segment glass transition temperature is unaffected by the addition of clay while the thermomechanical and thermal degradation behavior is inconsistent and depends heavily upon the interactions between the clay, chemical modification, and polyurethane. Furthermore, the greatest thermomechanical, thermal, and barrier enhancements are exhibited in the nanocomposites with the best clay dispersal [54].

These publications also suggest that the reinforcement capability of the clay depends primarily upon the dispersal of the clay and that the type of clay is of lesser importance [58-60]. The clay dispersal tends to be best in soft polyurethanes, those containing less than 50 wt% hard segment, because it is more difficult for the rigid hard segments to diffuse between silicates [37]. While the melt processing-based dispersal technique may be more environmentally friendly than using a common solvent, the high temperatures needed for the melt can cause the chemical modification of the clay and polyurethane to interact unfavorably and deteriorate the mechanical properties of the polyurethane [46]. If the common solvent technique is used, the clay is best dispersed when the solution is sonicated [48]. Unfortunately, in all of these publications the intercalation of the large aspect-ratio clays investigated has persisted and the maximum thermomechanical, thermal, and barrier enhancements have been exhibited at small clay weight concentrations.

Ultimately, in order to develop a polyurethane/clay nanocomposite that exhibits a large increase in stiffness and strength, good dispersal of clay is necessary. To avoid possible deleterious interactions between clay chemical-modification and polyurethane, a dispersal technique that does not rely upon the chemical modification of the clay is needed. Furthermore, the reinforcement capabilities of smaller aspect-ratio clay need to be evaluated. Small aspect-ratio clays may be more easily dispersed and the thermomechanical enhancements could prove interesting since smaller aspect-ratio clay is less likely to shield the polyurethane from straining [54].

of Laponite to DMAc was greater than 0.70 wt%. At concentration higher than this the resultant solution does not reliably dissolve the polyurethane. When concentrations greater than 0.70wt% were made heat was necessary to dissolve the polyurethane in solution. Occasionally, even after a few hours at an elevated temperature as high as 140°C, the solution appeared to be emulsion-like and cloudy rather than completely dissolved and the resultant films were lumpy and discontinuous. This emulsion-like state may indicate that at Laponite weight fractions greater than 0.007 in DMAc, the system is more of a gel rather than an effective solvent. To avoid instances such as these, concentrations below 0.70 wt% were used.

This DMAc-Laponite solution was then mixed with various quantities of pure DMAc and approximately 0.33 g of polyurethane in 60 ml, thick-walled, glass vials. The total amount of solution necessary was determined by the mass of the polyurethane in the vial and the desired polyurethane concentration in solution, which was approximately 1.5 wt%. Concentration has a dramatic affect on material properties and therefore was kept constant from one nanocomposite to the next. Nanocomposites containing, 0, 1, 2, 4, 6, 8, 10, 15, and 20 wt% Laponite in Elasthane were made. The amount of DMAc-Laponite mixture was determined by the desired Laponite concentration in polyurethane. The amount needed could be calculated by solving the following equation

$$\phi_m = \frac{CA}{CA + m_{PU}}, \quad (4.1)$$

where ϕ_m specifies the weight fraction of Laponite in the PU desired, C is the resultant weight fraction of Laponite in the DMAc-Laponite mixture, m_{PU} is the mass of the polyurethane, and A is the mass of the DMAc-Laponite mixture needed. The mass of pure DMAc needed is determined by taking the difference between the total mass of solvent needed less the mass of the of the DMAc-Laponite mixture needed. The resultant PU-DMAc-Laponite mixture was then rolled on a Wheaton mixer for 24 hours or until the PU was completely dissolved. In a few instances when the concentration of Laponite in DMAc was excessively high (≥ 0.70 wt%) or when the HDI-based PUs were used it was necessary to heat the solutions to 140°C for 3-6 hours. After complete dissolution the solution was sonicated at room temperature for 60 minutes. At this point, each vial contained a transparent PU-DMAc-Laponite mixture in which the Laponite was fully exfoliated as will be shown in the resultant nanocomposite x-ray diffraction data presented in Chapter 5.1.

4.1.3 Preparation of Thin-film Nanocomposites

After the PU-DMAc-Laponite solutions were prepared, following the procedure outlined in the previous section, PU/clay nanocomposite thin films were prepared. This was accomplished by utilizing a Teflon block that had an interior cut-out 4 cm in width and 6 cm in length and 4 cm in height as shown in Figure 4.7.

Each PU-clay-DMAc mixture was pipetted into the block so that after all DMAc was removed at the least 0.3 g of PU would remain. Because the PU-clay-DMAc mixture had a PU concentration of c.a. 1.5 wt% approximately 19 g of solution was needed to make one thin film. Once the solution was placed in the Teflon block and the mass recorded, the block was immediately put in a 60°C oven with a N₂ purge of 0.023 ± 0.005 m³ hr⁻¹. Typically, the DMAc was completely removed in 10-12 days. The block was only removed from the oven when

inspection showed all the solvent appeared to be gone. This was verified by measuring the mass of the Teflon block containing the PU/clay composite and ensuring the change in mass from that measurement prior to heating was greater than or equal to 99% of the expected loss. If less than 99% of the solvent was removed the block was placed back in the oven until the value was surpassed or in a few cases no more mass loss occurred.

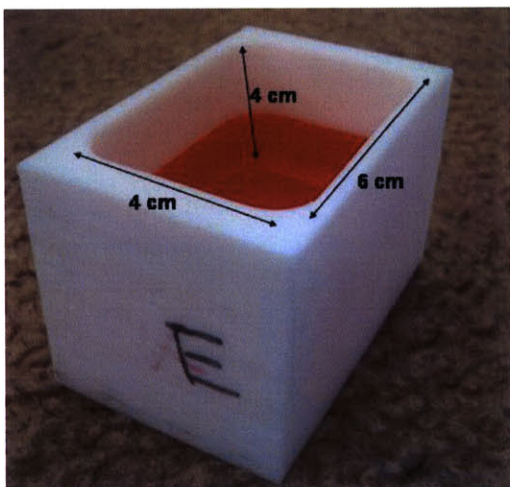


Figure 4. 7: Photograph of the Teflon block filled with red dye to elucidate the internal dimensions.

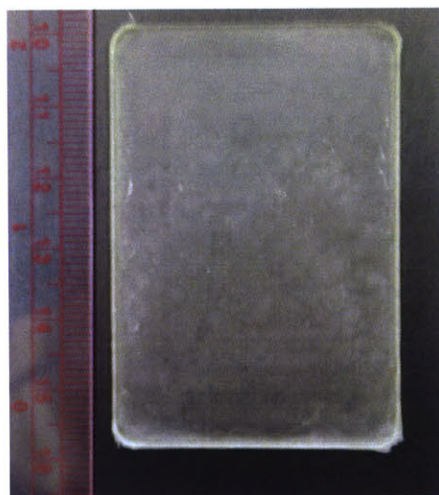


Figure 4. 8: Photograph of a thin-film polyurethane/Laponite nanocomposite removed from the Teflon plate after drying.

It should be noted that other procedures for removing the solvent were investigated, including using a vacuum and air drying. The vacuum proved hard to regulate. Under vacuum, bubbles often nucleated in the PU solution and upon drying, these bubbles created cavities on top of the thin film or created air-pockets within the thin film. Air drying proved to be too slow and despite stringent efforts, large dust particles found a way to contaminate the solution. Furthermore, the solvent removal rate seemed to change the mechanical properties of the nanocomposite. Therefore, the use of an oven at 60°C with a N₂ purge afforded a well-regulated procedure. The 60°C temperature was chosen because it was below the PU hard segment melting temperature and because it is considered a kinetically favorable annealing temperature for PUs [69].

After removal from the oven, the Teflon blocks were cooled at room temperature and the thin films covered. Once cooled, the thin films were carefully peeled away from the Teflon, weighed, and placed in Petri dishes that were kept in a desiccator. After at least 24 hours in the desiccator, the thin films were cut into narrower strips (~60 x 5 x 0.1 mm³) using a custom cutter and readied for characterization. Note, all characterization was performed within 24 hours to 30 days after film placement in the desiccator, but all mechanical testing was completed within the 6-14 day range to ensure no degradation affects.

4.2 Characterization Methods

This section describes the operating concept behind each characterization method utilized and then describes the test procedure followed.

4.2.1 Transmission Electron Microscopy

Transmission electron microscopy was performed in order to obtain visual images displaying the extent of the Laponite dispersal in polyurethane.

4.2.1.1 Operating Concept

Transmission electron microscopy is an imaging technique that allows materials to be interrogated via their electron densities. A thermionic electron gun shoots electrons at a material specimen. When electrons collide with the material there are three possible outcomes: 1. the electrons pass through because there is no atomistic interaction, 2. the electrons deflect elastically, losing no energy, or 3. the electrons deflect inelastically, transferring energy and exciting secondary electrons [70]. An objective aperture placed on the through side of the material filters out the scattered electrons so that only those electrons that passed through the sample are imaged. Consequently, those materials composed of light atoms like carbon allow a lot of electrons to pass through without deflection and appear as bright fields, while heavy atoms like lead, deflect most of the electrons and appear as dark fields [70].

4.2.1.2 Test Procedure

The transmission electron microscopy (TEM) was performed at the Center for Materials Science and Engineering at MIT on a JEOL 200CX TEM operated at an accelerating voltage of 200kV. Prior to TEM imaging, thin cross-sections of the nanocomposite must be prepared, cryotomed, and stained. Because the electron densities of the hard and soft polyurethane segments are similar, typically polyurethane samples are stained with osmium tetroxide (OsO_4) in order to distinguish the hard segments from the soft segments. However, not only is staining PUs difficult, but the staining interfered with the identification of the higher electron density Laponite and was avoided after an initial trial.

To prepare the nanocomposite for cryotoming, 30° - 60° - 90° triangular, thin-film nanocomposite sections were cut so that the longest side was approximately 3 mm and fit in the cryotome post shown in Figure 4.9. These unstained triangles were placed in the flat slot of a flat-head threadless screw (head diameter of 3 mm, pin diameter of 2 mm, and total length of 10 mm) with a drop of 5 minute epoxy. Care was taken to ensure that the triangle stood out perpendicularly from the flat slot in the pin head as shown in Figure 4.9.



Figure 4. 9: Photograph of the nanocomposite thin-film fixed with epoxy upon a cryotome post.

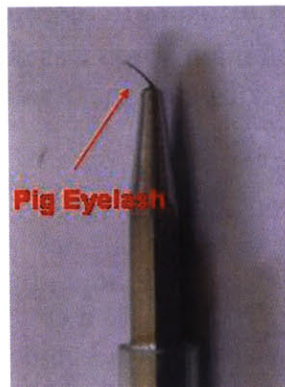


Figure 4. 10: Photograph of the pig eyelash used to place the cryotomed sample on the carbon mesh.

After at least 24 hours the sample, on its peg, was brought to the lab and cryotomed. After cutting away the initial epoxy covered triangular tip, ~ 100 nm thick sections were prepared using a MT- χ Cryo-Ultramicrotome with a diamond knife. The peg fit into the cryotome sample holder and was aligned and locked down. The chamber was kept at -170°C using a dewar filled with liquid N_2 during sectioning. The cryo-diamond knife used was provided by the Hammond Group (EM Corp. knife No. 1289 M with a 45° included angle, a 4° clearance angle and a 3.0 mm length). The cutting speed used to make long, continuous, thin sections was 0.1 mm s^{-1} . The samples were collected and positioned on 200 mesh copper grids with the pig eyelash pictured in Figure 4.10.

The samples were then ready for examination in the TEM. After image exposure the film was developed in the dark room using the specified procedure. The dry negatives were scanned onto a computer and saved at their original size at the highest resolution possible and then analyzed.

4.2.2 Atomic Force Microscopy

Tapping-mode or intermittent-contact atomic force microscopy phase images [71] were used to identify the topographical dispersal of hard Laponite within the soft polyurethane matrix.

4.2.2.1 Operating Concept

An atomic force microscope (AFM) is a type of scanning probe microscope that uses the relation between interatomic forces and distance to investigate the topography and topological material properties of a specimen [72]. The AFM can operate in one of three modes, contact mode, non-contact mode, or intermittent-contact mode, by adjusting the distance between the probe tip of the AFM and a specimen. The probe tip is attached to a cantilever that is sensitive to the various sample-tip interactions and the resultant cantilever behavior is monitored and characterized in order to elucidate the topographical nature of the sample [72].

In contact mode the tip is repelled by the atoms of the specimen via van der Waals forces. Consequently, the flexible cantilever bends upward and the deflection is measured by an intricate optical detection system. Therefore, the tip can be traced across the sample at a constant height and the deflection monitored to elucidate the specimen relief or the deflection can be monitored

and the height position of the tip changed so that the tip scans the specimen at a constant force [72].

In non-contact mode the tip is held far enough away from the specimen (10-100 Å) that the tip-specimen atomic interactions are small and attractive (10^{-12} N) [72]. In this mode a stiff cantilever is vibrated near its resonant frequency and changes in the frequency are detected as the tip moves across the specimen. Because the cantilever-resonant frequency depends on the square root of the spring constant which in turn varies with the attractive van der Waals force gradient applied by the sample, the sample topography can be determined [72].

In intermittent-contact mode the cantilever is again vibrated, however, the tip to sample distance is smaller than that in non-contact mode. In this instance the tip is held at a distance that allows the tip to just touch the sample when the cantilever is deflected downward during vibration. Changes in the oscillation amplitude of the cantilever correspond to changes in tip-sample separation. So by monitoring the oscillation amplitude the topography of the specimen can be determined [72].

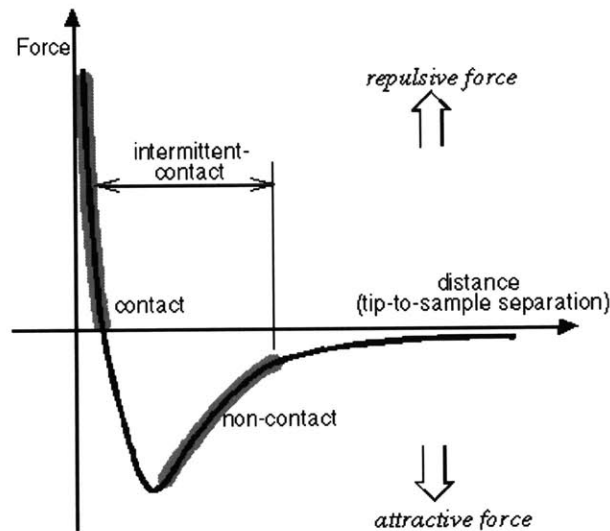


Figure 4. 11: AFM operating regions displayed on an interatomic force versus distance curve as presented in [72].

In non-contact mode or intermittent contact mode, while topographical information is being collected, phase detection information can be collected simultaneously. Phase detection is a technique that measures the phase lag between the input signal which initially drives the cantilever oscillation and the output signal, which changes the initial oscillation depending on the tip-specimen interactions. Changes in phase lag correspond to changes in the material stiffness or rigidity [72]. Consequently, in one scan of a sample two images can be obtained, one depicting the topography of the sample scanned and the other depicting the hard and soft regions within that height survey.

4.2.2.2 Test Procedure

Atomic force microscopy was performed using a Nanoscope Dimension 3100 scanning probe microscope from the Veeco Metrology Group in tapping mode. The TEM grids holding

cryotomed sections were attached to magnetic sample holders using double-sided scotch tape and the surface of the nanocomposite was analyzed. The tips used were provided by Digital Instruments and are rotated tapping-mode etched silicon probes (RTESP) that have a resonant frequency of 300 kHz and a spring constant of 40 N m⁻¹.

4.2.3 Wide Angle X-Ray Diffraction

Wide angle x-ray diffraction was performed to determine the extent of the Laponite dispersal within the polyurethanes at various Laponite concentrations.

4.2.3.1 Operating Concept

X-ray diffraction is an experimental technique that distinguishes crystalline structures in materials. When x-rays are transmitted to and collide with atoms of an amorphous material specimen, the electrons surrounding the atoms begin to oscillate at the same frequency as the arriving x-ray, but the x-ray emissions are out of phase. Consequently, destructive interference dominates in most directions and no energy or beam emissions appear to exit the sample [73]. However, if the atoms are in a crystal or regular order a number of directions emit waves that are in phase, constructive interference dominates, and diffracted x-ray beams are emitted increasing the intensity which is detected.

In the Bragg-Brettano mode an x-ray tube emits the x-rays at one constant location and the specimen rotates through Bragg angles (θ_B) from 0° to 40° at half the speed the detector rotates through scattering angles (θ_S) from 0° to 80° [73]. The detector records the intensity of the x-rays emitted at each Bragg angle, and when crystalline structures are present there are peaks in intensity. The peaks in intensity at various Bragg angles correspond to various crystalline interplanar spacing or d -spacings according to Bragg's Law (visually described in Figure 4.12) which is defined as

$$d = \frac{n\lambda}{2 \left(\sin(\theta_B) \right)}, \quad (4.2)$$

where λ is the wavelength of the x-ray emitted (~1.54 Å), d is the distance between crystalline planes, n is a positive integer, and θ_B is half of the scattering angle. Consequently, intensity peaks at small Bragg angles correspond to large d -spacings, while peaks at large Bragg angles correspond to small d -spacings. Each crystalline or ordered structure has its own unique diffraction pattern, which can be utilized to examine materials like polymers which contain a variety of polycrystalline components which each have their own different diffraction signature [73].

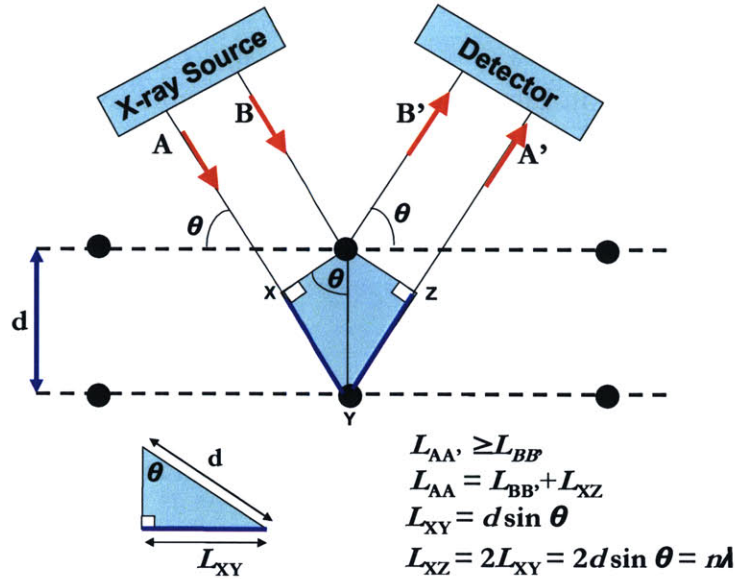


Figure 4. 12: Diffraction image describing the derivation of Bragg's Law

4.2.3.2 Test Procedure

X-ray diffraction was performed using a Rigaku RU300 with an 18 kW rotating CuK α anode x-ray generator, a 185 mm diffractometer, and a scintillation counter, in the Bragg-Brettano mode at the Center for Materials Science and Engineering at MIT and was performed by Joe Adario. The thin film samples approximately 10 x 5 x 0.1 mm³ were attached to a silicon background using very small strips of scotch tape at the edges. The pure Laponite powder was ground more finely in a mortar and pestle and then pressed into the 18 x 20 x 0.3 mm³ window in a glass sample holder. The tests were performed using a 0.5° divergence slit, a 0.5° scatter slit and 0.15 mm receiving slit. Each sample was tested at angles from 2° to 80° at 5° min⁻¹ with a 0.05° sample interval.

4.2.4 Thermogravimetric Analysis

Thermogravimetric analysis was performed to verify that the nanocomposites contained the specified Laponite loading and to elucidate the affect of Laponite concentration on the thermal degradation of the polyurethane.

4.2.4.1 Operating Concept

Thermogravimetric Analysis (TGA) is used to determine the degradation temperatures of polymers, the amount of residual solvent or water left in polymers, and the amount of incombustible, inorganic filler left in polymers [74]. The instrument consists of a sample pan that is attached to a sensitive microbalance and then sealed within a high temperature furnace. The temperature in the furnace can be programmed to either remain constant or increase at a specified rate. As the sample is thermally loaded the microbalance measures the mass of the sample placed in the pan as a function of time and temperature. Typically the mass loss curves are used to determine the temperature at which various degradation processes occur, to determine the mass loss at a specified temperature, and/or to determine the amount or percent of non-combusted residue (char) left at a specified final temperature [74].

4.2.4.2 Test Procedure

The thermogravimetric analysis was performed at the Center of Materials Science and Engineering at MIT on a Perkin Elmer TGA7 with a 20 ml min⁻¹ N₂ purge. Platinum pans were filled with between 6.1 and 7.8 mg of nanocomposite material cut with a razor into small pieces measuring approximately 3 x 3 x 0.1 mm³ and placed flat against the pan bottom. When the mass was equilibrated and finally showed no deviation due to slight pan swinging the test was started. The test included a 1 min isothermal hold at 30°C and then a 10°C min⁻¹ ramp to 1000°C and another 5 min isothermal hold at 1000°C. The mass loss profile of the sample during heating was recorded and analyzed.

4.2.5 Differential Scanning Calorimetry

Differential scanning calorimetry was performed to determine the affect of Laponite concentration on the glass, melting, and crystallization transitions of the block-polymeric polyurethane nanocomposites.

4.2.5.1 Operating Concept

Differential scanning calorimetry (DSC) is a technique used to measure the heat flux associated with material transitions which are both time and temperature dependent. The material heat flow is quantified by comparing the difference in heat flow between a sample-filled pan and an empty pan that are subject to the same time, temperature, and pressure test conditions [75].

As depicted in Figure 4.13, two sealed pans, one filled with sample and the other, an empty reference pan, are placed in a chamber and heated simultaneously by the same source, a thermoelectric disk. Thermocouples are connected in series and placed at the pan locations, between the chromel discs and the thermoelectric disc, where they are used to measure the differential heat flow between the two pans. Each thermocouple is comprised of a chromel and alumel wire pair which will exhibit a voltage change in the circuit if the temperature at their junction differs from a reference temperature[75]. From these voltage changes the temperature at each pan location can be back-calculated and using the thermal equivalent of Ohm's law the differential heat flow,

$$\frac{dQ}{dt} = \frac{T_{Sample} - T_{Ref}}{R_D}, \quad (4.3)$$

where R_D is the thermal resistance of the thermoelectric disc, is determined. The resultant heat flow can be plotted against temperature and the inflections which indicate glass transitions and the endothermic peaks which indicate melting and exothermic peaks which indicate crystallization evaluated [75].

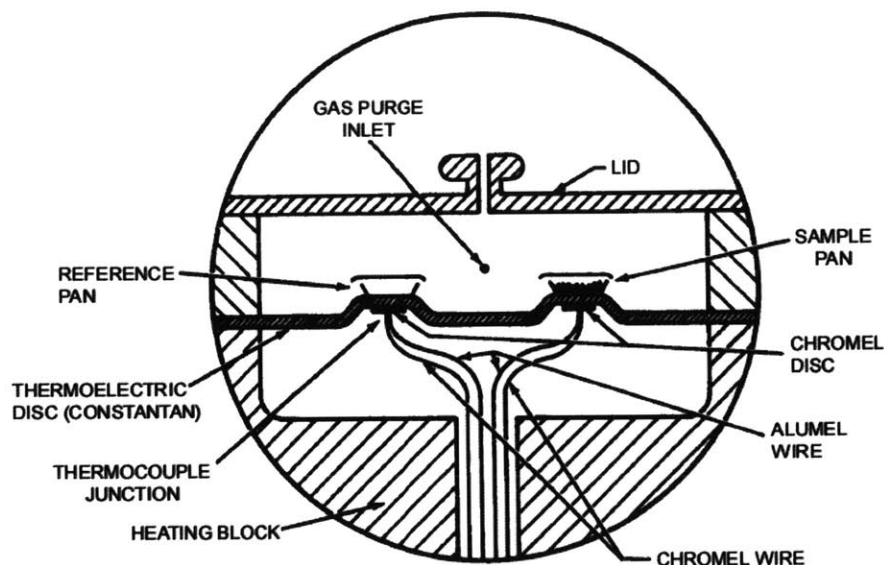


Figure 4. 13: Heat flux DSC Schematic as shown in [75].

Modulated DSC is used to examine the complex material transitions seen in conventional DSC curves. It separates overlapping events in the heat flow curve into reversible (i.e. glass transitions) and nonreversible (i.e. crystallization) components. The heat flow recorded in conventional DSC is equal to the sum of reversible and irreversible components,

$$\frac{dQ}{dt} = c_p \beta + f(T, t), \quad (4.4)$$

where c_p is the heat capacity, β is the average underlying heating rate, and $f(T, t)$ is the heat flow due to irreversible kinetic processes [75]. Unfortunately, in conventional DSC only one linear heating or cooling rate can be applied and these test conditions do not provide enough information to decompose the resultant heat flow into separate components. However, in modulated DSC a sinusoidal oscillation is laid atop the conventional linear heat ramp and offers a second heating rate that can be used to determine the reversible heat capacity component of the heat flow. The heat capacity is determined by dividing the difference in modulated heat flow amplitudes between the sample pan and the reference pan by the modulated heating rate amplitude and multiplying that value by a calibration constant. Then the irreversible kinetic component is equal to the difference in the differential heat flow and the reversible heat flow [75, 76].

When modulated DSC is used the temperature ramp can be as fast as $100^\circ\text{C min}^{-1}$ like in conventional DSC and the modulation period can be within 10 s to 100 s while the temperature oscillation amplitude can range within ± 0.01 - 10°C . However, the conditions should be chosen so that at all instants the heating rate is greater than or equal to 0°C min^{-1} [76]. It is important that 0°C min^{-1} is the minimum instantaneous heat rate so there is no chance of affecting crystallization phenomena and so the irreversible heat flow is guaranteed a result of kinetic phenomena not heat-capacity affects. When running modulated DSC the test conditions should be chosen so that the longest period possible is utilized, but the heating rate should be chosen so that at least four modulation cycles occur within the transition region investigated [76]. The

correspondence between the heating rate, H_R [$^{\circ}\text{C min}^{-1}$], the period, P [s], and the modulated temperature amplitude, T_{AMP} is

$$T_{AMP} = H_R \frac{P}{2\pi(60)}. \quad (4.5)$$

4.2.5.2 Test Procedure

To evaluate the thermal behavior of the nanocomposites between -90°C and 250°C a TA Instruments Q 1000 series DSC with a 50 ml min^{-1} N_2 purge was utilized. Aluminum pans were filled with 4-6 mg of thin film pieces that had been cut with a razor into small squares (3 mm x 3 mm) and placed flat against the bottom of the pans. Aluminum lids were placed atop the pans and the combo was crimped shut using the TA sample encapsulation press.

Before a set of DSC tests were run, a baseline test was performed. This entailed running one cycle of the test that would be used on the nanocomposite filled pans with no pans in the test chamber. The resultant heat flow should be flat or at have a slight constant slope close to 0 mW and not contain any spikes or anomalous behavior. Spikes and other anomalous behavior indicated that the test chamber had been contaminated by a previous test, so the chamber was cleaned, the residue chemicals or water were burnt off, and another baseline was run. This procedure was repeated until the baseline was flat or slightly sloped and displayed no spikes or anomalous behavior.

Once a good baseline had been achieved the nanocomposites were tested. The standard test performed was a two cycle, $10^{\circ}\text{C min}^{-1}$ ramp, where one cycle consisted of a ramp from -90°C to 250°C , an isothermal hold for 3 min at 250°C , a ramp back down to -90°C , and another isothermal hold at -90°C for 3 min. The first cycle exhibits irreversible melting transitions while the second cycle exhibits an equilibrium behavior conducive to these test conditions.

To elucidate the irreversible hard segment transitions above 50°C , modulated temperature DSC was performed. In this instance the temperature was ramped just once from 50°C to 250°C at $2^{\circ}\text{C min}^{-1}$ and the modulation period was set to 60 s. These conditions correspond to a 0.318°C temperature amplitude.

In a later analysis the soft segments of the various PUs were mixed with varying quantities of Laponite and then sealed within hermetic aluminum pans and their thermal behavior analyzed between -90°C and 125°C in two DSC cycles at a $10^{\circ}\text{C min}^{-1}$ ramp rate.

4.2.6 Dynamic Mechanical Analysis

Thin film dynamic mechanical analysis was performed to determine the affect of Laponite concentration on the nanocomposite thermomechanical properties.

4.2.6.1 Operating Concept

Dynamic mechanical analysis (DMA) is performed on polymers in order to determine the elastic energy storage and viscous energy dissipation properties of the polymer as a function of time and temperature. In thin-film DMA a polymer film is held in tension with its top end connected to a stationary clamp and the other end attached to a clamp on an oscillating, retractable drive shaft [77]. The entire assembly sits within a furnace. The oscillating stress or strain amplitude, oscillating frequency, and temperature can all be controlled and the thin-film thermomechanical properties, i.e. the flexural storage modulus, the flexural loss modulus, and the loss tangent, are determined and material thermal transitions are inferred.

The stress, σ , is defined as

$$\sigma = \sigma_o \sin(\omega t) \text{ or } \sigma^* = \sigma_o \exp(i\omega t), \quad (4.6)$$

where σ^* is the complex stress, σ_o is the stress amplitude, ω is the frequency of oscillation in rad s^{-1} , and t is time. Similarly, the strain, ϵ , is defined as

$$\epsilon = \epsilon_o \sin(\omega t - \delta) \text{ or } \epsilon^* = \epsilon_o \exp\{i(\omega t - \delta)\}, \quad (4.7)$$

where ϵ^* is the complex strain, ϵ_o is the strain amplitude and δ is the phase angle which describes the lag time between the stress and strain oscillations. The complex flexural modulus, E^* , is the ratio of the complex stress to the complex strain,

$$E^* = \frac{\sigma^*}{\epsilon^*} = \frac{\sigma_o}{\epsilon_o} \cos(\delta) + i \frac{\sigma_o}{\epsilon_o} \sin(\delta) = E' + iE''. \quad (4.8)$$

The complex flexural modulus can be broken into real and imaginary components where E' represents the flexural storage modulus and E'' represents the flexural loss modulus. The storage modulus quantifies the elastic behavior of the material while the loss modulus quantifies the viscous behavior of the material. The ratio of the elastic behavior to the viscous behavior is the loss tangent ($\tan \delta$). Peaks in the $\tan \delta$ curve correspond to glass transition temperatures, however, these values differ from those observed in DSC due to differences in experimental procedure [78].

A dynamic mechanical analyzer calculates these properties similarly; however, correction factors and approximations are used to account for the limitations of the instrument. Ultimately, thermomechanical properties can be plotted as a function of temperature and frequency and the behavior of the material analyzed [79].

4.2.6.2 Test Procedure

The flexural moduli, the soft segment glass transition temperature (T_g), and the dissipation factor of the nanocomposites were determined via dynamic mechanical analysis (DMA) using a TA Instruments Q 800 series DMA over a temperature range of -100 - 250°C at a frequency of 1Hz, a ramp rate of 3°C min^{-1} , and an initial strain of $\sim 0.2\%$. Thin films were typically $13 \times 5 \times 0.1 \text{ mm}^3$ and the amplitude specified in the test set-up was set at $30 \mu\text{m}$ and/or $45 \mu\text{m}$. At least two tests were performed to ensure good repeatable results. It should be noted that before a set of testing the machine was calibrated and the offset was between 0.254 and 0.272, meaning that results from one day to the next were comparable and at the most may exhibit 10% error.

4.2.6.3 Static Thermomechanical Analysis

In order to capture a more visual understanding of the difference in heat distortion behavior, 0 wt% and 20 wt% Laponite-filled nanocomposites were compared in a side by side laboratory experiment. The two films were approximately $55 \times 5 \times 0.1 \text{ mm}^3$ and were clamped between glass slides using paper clamps 5 mm from the thin film end. The top clamp of each film was tied to a rod which extended perpendicularly from a ring stand, which was placed in a large oven with a window in its door at a temperature of 45°C . Then 110 g weights were attached to the bottom clamp of each film, which was equivalent to a 1.7 MPa initial stress, and the oven door closed. Photographs of the set-up are displayed in Figures 4.14 and 4.15. After thirty minutes the thin films stopped their slight swinging which was induced when the weights were attached. At this time there was no apparent change in length of either thin film. At this point the temperature of the oven was ramped from 45°C to 125°C at a little better than 1°C min^{-1} and digital images were captured, recording the nanocomposite behavior every 5°C and at critical events.

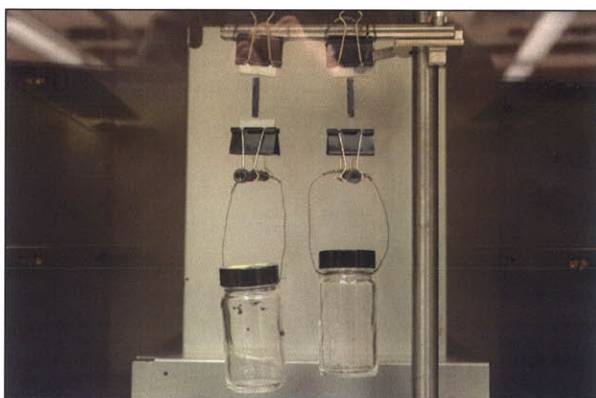


Figure 4. 15: Heat distortion comparison of pure Elasthane and 20 wt% Laponite-filled Elasthane experimental set-up.

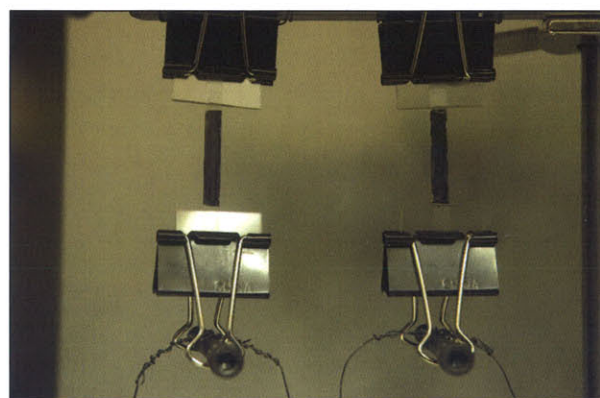


Figure 4. 15: Heat distortion comparison set-up zoomed view (pure Elasthane—left, 20 wt% Laponite-filled Elasthane—right).

4.2.7 Zwick Mechanical Testing

Tensile tests were performed on the thin-film nanocomposites to determine the affect of Laponite concentration on the stiffness, toughness, extensibility and ultimate strength of the polyurethanes.

4.2.7.1 Operating Concept

Mechanical tensile or compression testers hold a material at one end and stretch or compress the material at the other end at some specified rate and record the force applied during the deformation of the material. Three outputs can be obtained from these mechanical tests, elapsed time, the distance traveled by one end of the tester, and the force applied. The force-deformation information collected in a tensile test can be manipulated into an engineering stress-strain curve.

Engineering stress, σ , is defined as

$$\sigma = \frac{F}{A_o}, \quad (4.9)$$

where F is the force recorded and A_o is the initial cross-sectional area of the material tested. The engineering or nominal strain, ϵ , is defined as

$$\epsilon = \frac{\ell - \ell_o}{\ell_o}, \quad (4.10)$$

where ℓ is the material length and ℓ_o is the initial material length. The true strain, ϵ_{True} , is defined as

$$\epsilon_{True} = \ln\left(\frac{\ell}{\ell_o}\right) = \ln(1 + \epsilon). \quad (4.11)$$

Unfortunately, true stress can not be calculated without knowing the material compressibility or having another measurement of the material deformation in a second dimension [78]. From the stress-strain information the mechanical properties, such as elastic modulus, ultimate strength, extensibility and toughness can be calculated.

The elastic modulus, E , of polymeric material is typically defined as the slope of a line passing through the initial linear regime of a stress-strain curve. The ultimate strength is the highest stress achieved prior to material failure; however, the two points often coincide. The extensibility is defined as the failure strain. The toughness is defined as the area under the stress-strain curve [80]. These four properties are shown in the diagram depicted in Figure 4.16.

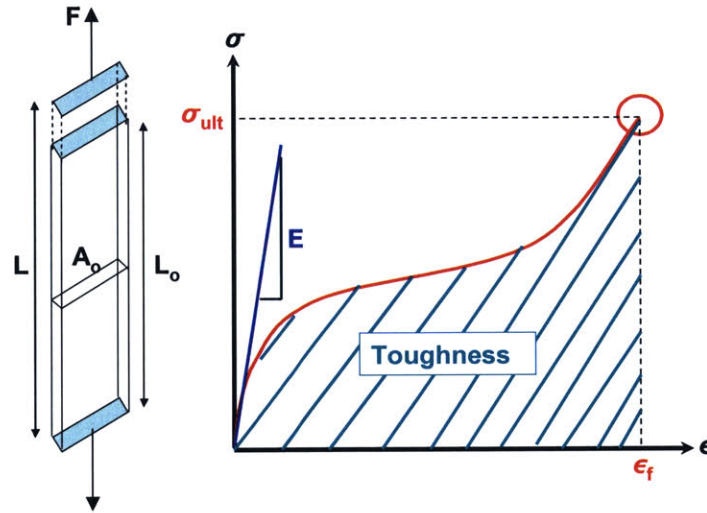


Figure 4.16: Demonstrative engineering stress-strain curve and depiction of the mechanical properties calculated.

4.2.7.2 Test Procedure

Tensile tests were performed on thinfilm samples approximately $45 \times 5 \times 0.1 \text{ mm}^3$ using a Zwick/Roell Z010 mechanical tester with a 500 N load cell at a constant crosshead speed of $100\% \text{ initial length min}^{-1}$ until film failure. The grips used were provided by Zwick/Roell and fall under the part number 8133.00. These grips have a mechanism within them that tightens the grip under increased load; consequently, to ensure failure occurs in the middle of each thin film the grips were manually screw-tightened a little less than finger tight. The pair of jaw faces that

fit within each grip includes one convex aluminum face and one flat polyurethane face. The grip and jaw face combination are now referred to as the “MIT grips” at Zwick/Roell. Prior to testing the thin films were placed in the middle of the jaw faces and the slightest bit of slack was maintained so that the material was not pre-stressed. A 0.015 N pre-load was applied at the onset of each test to ensure regularity between tests. At least three samples were tested at each Laponite concentration in order to obtain good error estimates.

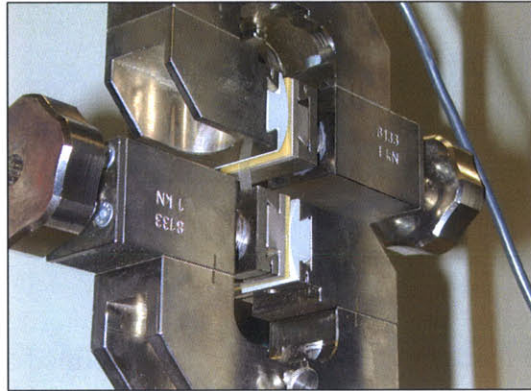


Figure 4. 17: Photograph of the Zwick/Roell thin film grips.

4.2.8 Optical Microscopy Using Cross-Polarized Light

Not only can optical microscopes be used to examine the micron-size topographical structures of thin films, but by utilizing cross-polarized light, the aligned or oriented crystalline and anisotropic or birefringent structures within the film can be distinguished from the amorphous regimes.

4.2.8.1 Operating Concept

Light is essentially a collection of electromagnetic waves that oscillate perpendicular to the line of propagation. When monochromatic light waves collide with a polarizer only those waves that are parallel to the polarizing plane are allowed to pass through. Then the parallel waves pass through the specimen analyzed and enter an analyzer, another polarizing filter that can be rotated from 0° to 90° . When there is no specimen present and the analyzer is at 0° the light passes through the analyzer and exhibits a bright field. However, when the analyzer is at 90° the light is unable to pass through the filter and a dark field is displayed—the light is cross-polarized [81].

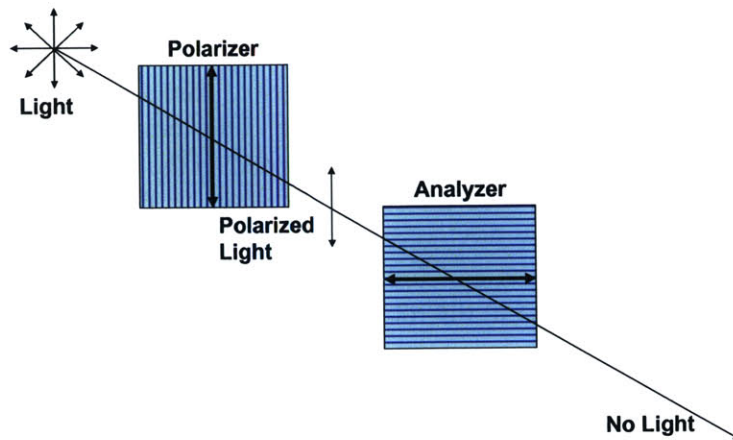


Figure 4. 18: Image depicting the path light travels through cross-polarized filters.

If instead a birefringent or anisotropic specimen is placed after the polarizer, the differing refractive indices of the specimen cause a unidirectional wave to split and rotate into two waves with different propagation speeds. The components of these waves which are parallel to the analyzer pass through and interfere with one another and display circular distributions of color with varying intensity. The inner circles, isochromes, consist of lower and lower order colors, according to the Michel Levy interference color chart [81]. As the sample is rotated the resultant colors and intensity may change. If the dark fields emitted remain dark through 360° of rotation the material can be identified as isotropic, rather than anisotropic. The brightly colored fields, isochromes, indicate changes in thickness, alignment, and stress [81]. If the sample is strained, isochromes will correspond to principal stress or strain differences and isoclinics correspond to the direction of principal stress or strain [82].

4.2.8.2 Test Procedure

The long range order, deformation, and crystalline morphologies of the nanocomposites before and after tensile tests were examined using a Carl Zeiss Axioskop 2MAT Polarizing Microscope with cross-polarized light. After mechanical testing, halves of the $45 \times 5 \times 0.1 \text{ mm}^3$ thin films used in tensile tests were carefully attached to glass slides using scotch tape. The thin film was attached to the slide at its ends and care was taken to make sure the thin film lied flat against the slide and that the film was not re-stretched or torn. Typically, it was easy to locate by eye the location where the grip held the film in the tensile test clamps. This line separated the stretched and aligned nanocomposite from the original structure prior to deformation and allowed easy comparison of the internal birefringent morphology. Digital images were captured at various magnifications, increasing the size of the original structures between 5 and 100 times.

In some instances films prior to deformation were examined and the bright field area calculated in order to determine the influence of Laponite or evaporation rate on the thin-film, long range, crystalline order. In these instances images were taken using the 5x objective and the exposure time and light intensity were kept constant. At least four images were taken of each film at a specified Laponite concentration. The images were then opened in Adobe Photoshop CS and the

color scale converted to a 16 bit grayscale. Each image was then inverted and the percentage of pixels that were below the 128 threshold was recorded.

In one study the pure and 10 wt% Laponite un-stretched thin films were placed on a hot plate that fit atop the examination area of the microscope. The temperature of the stage was set at 200°C and images of the thinfilm structure were recorded as the nanocomposite film transitioned from a solid to a liquid. The film was then brought down to 60°C and left there for 48 hours while the internal structures equilibrated and the film solidified. Again the internal, birefringent structures depicted under cross-polarized light were recorded at various times during annealing and the bright fields were examined in the manner mentioned previously.

4.3 Summary

The previous sub-sections of Chapter 4 described the experimental procedures followed to prepare and characterize the polyurethane/Laponite nanocomposites. The novel solvent exchange approach developed to fully disperse Laponite in three different polyurethane matrices, (a) Elasthane 80A, (b) PU-1-33, and (c) HDI-PTMO PU, was detailed. Furthermore, the operating concept and test procedures of the various characterization equipment used to evaluate the polyurethane/Laponite nanocomposites were described. TEM, AFM, and WAXD were used to evaluate the Laponite dispersal. TGA and DSC were used to evaluate the thermal degradation and thermal transition of the nanocomposites, while DMA was used to evaluate the thermomechanical properties. Uniaxial tensile tests were used to evaluate the mechanical properties of the nanocomposites and cross-polarized microscopy was used to interrogate the morphology of the nanocomposites. The following chapter will describe and discuss the results of the nanocomposite characterization.

Consequently, at this time it appears that the peaks observed in the second cycle of the 15 and 20 wt% Laponite-filled Elasthane heat flow curves corresponds to a new crystalline morphology. This behavior is consistent with the morphological change observed in the dynamic mechanical analysis loss tangent curves at these same Laponite concentrations. It is not yet clear how the Laponite is inducing this new crystalline morphology, however, it is clear from the DSC heat flow curves that the Laponite is disrupting the hard segment crystallinity.

Typically thermoplastic polyurethanes with MDI/BDO based hard segments have numerous melting endotherms the origin of which is still not entirely clear. Seymour and Cooper found that in a variety of polyester and polyether based polyurethanes three endotherms existed: a low-temperature endotherm due to short-range order at temperatures 20-30°C above the annealing temperature, an intermediate endotherm due to long-range order at 120-200°C, and a high temperature endotherm due to hard segment crystalline melting at 210-230°C [92]. Martin et al believes these endotherms correspond to the length of the hard segment, i.e. T_1 corresponds to single MDI segments, T_2 to MDI₂BDO, T_3 to MDI₃BDO₂, and so on while Chen et al suggest that the T_1 endotherm is actually an enthalpy relaxation behavior due to prolonged physical aging, and Saiani et al believe the intermediate endotherm corresponds to structures formed from microphase mixing of soft and hard segments [90, 91, 93]. Despite the confusion it appears that the increase in Laponite concentration as well as the nanocomposite preparation procedure significantly affects the location of the endotherms. The T_1 endotherm is constant and corresponds to the polyurethane preparation temperature at 60°C and the affect is erased upon heating to 250°C. The T_2 and T_3 endotherms are most influenced by Laponite concentration. Ultimately, the Laponite significantly impacts the long range ordering or microphase mixing of the polyurethane as well as the temperature, density, and intensity of the hard segment crystalline melting endotherms.

A comparison of the total and non-reversible modulated DSC heat flow curves of the Elasthane/Laponite nanocomposites confirms that upon heating the thin films, increases in Laponite concentration induce complex and irreversible melting and relaxation behavior. Because, as shown in Figures 5.21 and 5.22, the shapes and magnitudes of the total and non-reversible modulated DSC heat flow curves of each nanocomposite are so similar, it can be inferred that the melting and relaxation behavior observed at this time scale, which is on the order of minutes, is irreversible. Without more information it is difficult to correlate the changes in heat flow and increasing Laponite concentration to specific morphological changes or physical behaviors. It is obvious, however, that the long-range order and hard segment crystallite melting is significantly altered when the Laponite concentration is increased.

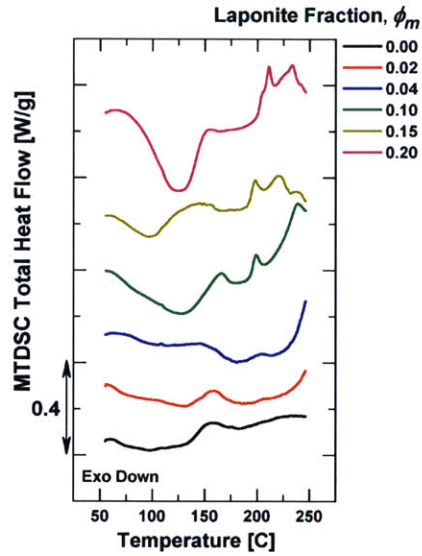


Figure 5.21: Modulated DSC heat flow of the various nanocomposites

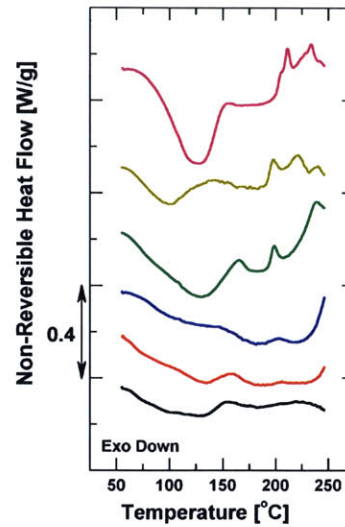


Figure 5.22: Modulated DSC non-reversible heat flow of the various nanocomposites

The previous DSC heat flow curves, specifically the cooling portion of the first cycle and the entire second cycle show that after heating to 250°C the well dispersed Laponite reduces the ability of the polyurethane to regain its short-range order and at very high concentrations induces a new melting and crystallization peak corresponding to a new morphology. Ultimately, the significant changes in the hard segment thermal behavior with increasing concentration of Laponite imply that the Laponite is embedded within or near the hard domain and has a significant impact on the hard segment melting behavior and crystallinity.

5.5 Evidence of Long Range Ordering

Evidence of long-range ordering or crystallization was apparent in cross-polarized microscopic images of the Elasthane/Laponite nanocomposites. The grip locale of a thin film that was tensile tested to failure is easily distinguished under cross-polarized light because the amorphous un-stretched material appears black, while the stretched material exhibits various colors of the spectrum depending on the extent of ordering, thinning, and the direction of alignment, as is shown in Figure 5.23. Within the amorphous un-stretched material, crystals like that shown in Figure 5.24, exhibiting three-dimensional fractal growth are apparent. These crystals vary in size and their lateral dimension measures between 100 and 200 μm , making these structures bigger than polyurethane hard domains which only measure between 10-30 nm in length [24]. Due to this discrepancy in size, at this time the origin of these crystallites has not been resolved.

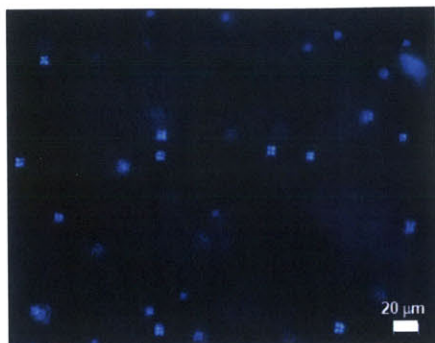


Figure 5. 38: Cross-polarized microscopic image of pure HDI-PTMO PU.

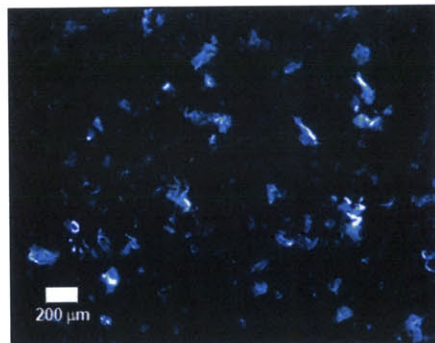


Figure 5. 39: Cross-polarized microscopic image of the HDI-PTMO PU filled with 10 wt% Laponite.

Maltese crosses were also apparent in PU-1-33 as well as larger, more irregular shapes that look similar to the Maltese crosses and other irregular, row-like crystalline structures as shown in Figure 5.40. As shown in Figure 5.41, when 10 wt% Laponite was added to PU-1-33 the row-like crystalline structures became more prominent while the Maltese crosses still existed but were not as easily observed. Therefore, the Laponite in the PU-1-33 system was not disrupting the hard domain crystallinity and not embedded within the PU hard domains.

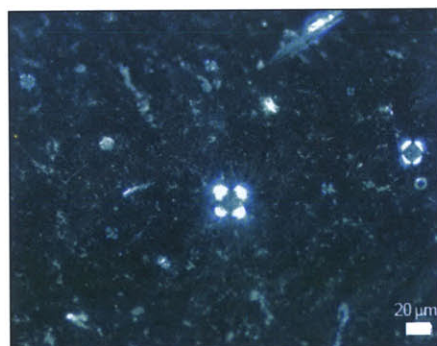


Figure 5. 40: Cross-polarized microscopic image of pure PU-1-33.

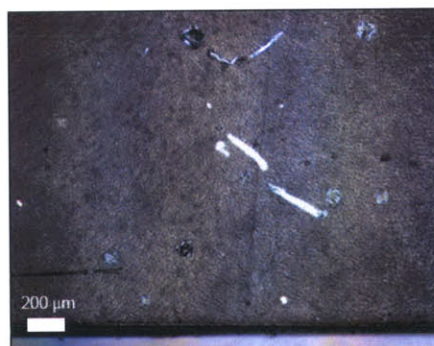


Figure 5. 41: Cross-polarized microscopic image of PU-1-33 filled with 10 wt% Laponite.

Ultimately, it is clear that the Laponite is preferentially embedded within the hard domains of the HDI-PTMO PU and within the soft domains of PU-1-33. Furthermore, the resultant crystalline structures induced by the Laponite are dependent upon the hard and soft segment constituents of the polyurethane and their respective interactions with the Laponite.

6. Conclusions

The novel solvent exchange approach used to exfoliate the Laponite nanoparticles in polyurethane matrices proved to be very effective. Transmission electron micrographs in conjunction with wide angle x-ray diffraction patterns above 5° indicated that the spacing between the basal planes of Laponite platelets was large and random, indicating good exfoliation (Figures 5.1-3).

The Elasthane/Laponite nanocomposites exhibited significant thermomechanical enhancement with increasing Laponite concentration. A thin film nanocomposite containing 20 wt% Laponite exhibited a 23-fold increase in elastic modulus, a 50% increase in strength, and nearly a 100% increase in toughness without loss of extensibility when compared to a pure Elasthane film (Figures 5.6-8). Furthermore, at a 20 wt% Laponite loading the heat distortion temperature increased by over 100°C from the value of 101°C measured for pure Elasthane (Table 5.1).

Characterization of the Elasthane/Laponite nanocomposites via mechanical testing, dynamic mechanical analysis (DMA), and differential scanning calorimetry (DSC) suggest that the dramatic thermomechanical enhancement is due to the preferential nanoreinforcement of the Elasthane hard domains with Laponite. Because the flexural storage modulus increases significantly at temperatures greater than the soft segment glass transition temperature ($T_{g,soft}$) and the soft segment glass transition temperature remains constant with increasing Laponite concentration, DMA suggests that the Laponite is embedded within the polyurethane hard domains (Figure 5.11). DSC further supports this hypothesis; the heat flow traces show disruption in the hard segment melting behavior but again no change in the soft segment glass transition with increasing Laponite concentration (Figure 5.18). Ultimately, the slow solvent removal utilized to prepare the polyurethane thin films allows the polyurethane nanocomposite to slowly self-assemble; the charge-deficient faces of the Laponite platelets are afforded time to preferentially pack amid the hard, polar domains of the polyurethane.

The results of characterization of two other polyurethane/Laponite nanocomposites suggest that by increasing the polarity and/or hydrophilicity of the polyurethane soft segment the Laponite can be directed away from the hard domain. When polyurethanes containing highly polar, hydrophilic soft segment constituents, such as polyethylene oxide (PEO), are employed the Laponite is directed away from the hard domains and embedded within the soft domain. The resulting material is less extensible and very brittle. The other two polyurethanes investigated both utilized the same hard segment at similar weight concentrations, but the soft segments, although of similar molecular weight, had different polarities and hydrophilicities. One polyurethane contained polytetramethylene oxide (PTMO) soft segments while the other polyurethane contained polyethylene oxide-polypropylene oxide-polyethylene oxide (PEO-PPO-PEO) soft segments. As can be seen from Table 6.1 PEO is more polar and has a higher solubility parameter than the other soft segment constituents.

Polyurethane	Soft Segment Constituent	Solubility Parameter [J ^{1/2} cm ^{-3/2}]
Elasthane	PTMO	18.039
HDI-PTMO PU		
PU-1-33	PEO	19.625
	PPO	16.873
	PEO-PPO-PEO	18.493

Table 6. 1: Polyurethane soft segment polarity expressed in terms of the solubility parameter which was calculated using the group contribution method and values given in [78].

Consequently, the novel polyurethane/Laponite nanocomposite that has a PTMO soft segment but hexamethylene diisocyanate (HDI) hard segment, behaves similar to Elasthane/Laponite nanocomposites, exhibiting an increase in strength, toughness, and stiffness without a loss in extensibility (Figure 5.33). Furthermore, like Elasthane nanocomposites, the HDI-PTMO PU nanocomposite exhibits a disruption in the hard segment crystallinity in DSC and a decrease in lossiness at the glass transition in DMA, but no change in the value of the soft segment glass transition temperature when Laponite is added (Figures 5.34, 36-37). Therefore, as in the Elasthane/Laponite nanocomposites, the Laponite is preferentially embedded within the hard domains of the HDI-PTMO PU and effectively strengthening and toughening the polyurethane.

The novel polyurethane/Laponite nanocomposite that has the same HDI-based hard segments but a more polar and hydrophilic, PEO-based soft segment exhibits contrasting behavior. The extensibility of the polyurethane (PU-1-33) is decreased dramatically when Laponite is added while the stiffness of the material exhibits no distinct change. The dramatic reduction in extensibility decreases the strength and toughness of the material significantly, and the nanocomposite behaves like a brittle plastic rather than as a stronger, tougher elastomer (Figure 5.33). Furthermore, DSC shows that the hard segment is unaffected by the addition of Laponite and although DMA shows that the value of the soft segment glass transition temperature is unchanged, the transition is broadened significantly, indicating a restriction in soft segment mobility (Figures 5.35-37). Characterization of this PU-1-33/Laponite nanocomposite suggests that the Laponite is embedded within the soft domain of PU-1-33, where it restricts soft segment mobility and negatively affects the extensibility of the material.

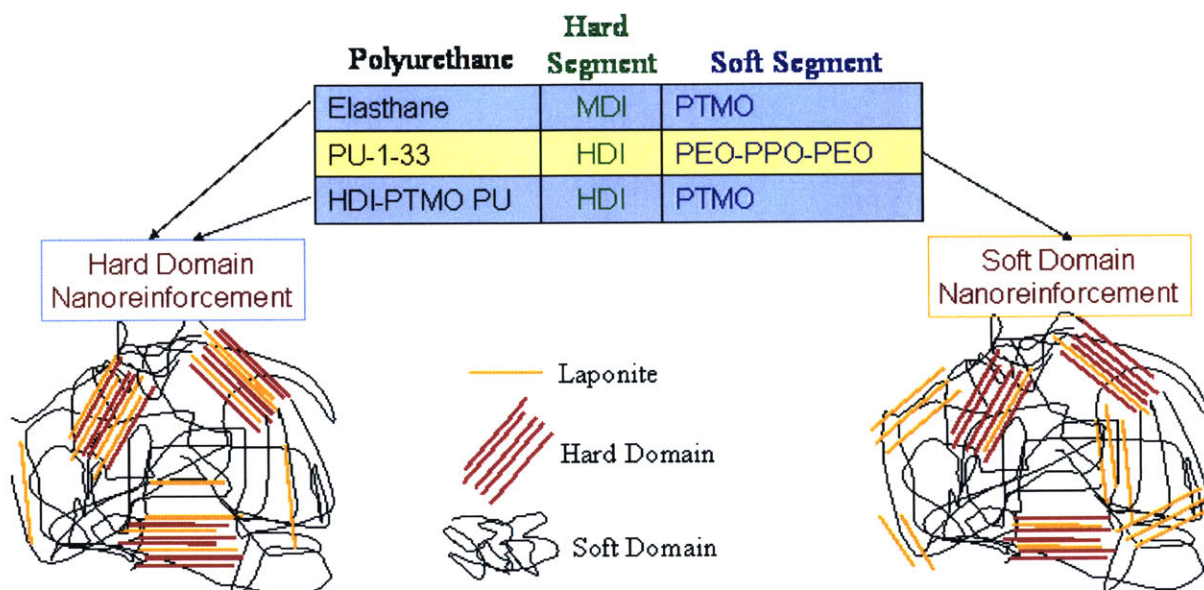


Figure 6. 1: Cartoon displaying the preferential location of Laponite in the various polyurethane nanocomposites investigated

Ultimately, when the novel solvent exchange approach is followed and the solvent removed slowly, the polyurethane has an extended period in which to preferentially self-assemble. Consequently, when the matrix of polyurethane/Laponite nanocomposites contains non-polar soft segments, the Laponite is preferentially embedded within the polyurethane hard domains, where it significantly enhances the thermomechanical properties of the material while maintaining material extensibility. As shown in Figure 6.1, a small fraction of Laponite may be embedded within the soft domain, but not enough to negatively influence the material behavior. However, when the matrix polyurethane contains polar constituents, such as PEO, the Laponite is preferentially embedded within the soft domain, restricting soft segment mobility and decreasing the material extensibility. Again, a small fraction of the Laponite may be embedded within the hard domain, but the Laponite within the soft domain dominates the material behavior. In summary, this novel solvent exchange approach and technique for nanocomposite preparation can significantly enhance the thermomechanical properties of polyurethanes which contain non-polar soft segments without hindering material extensibility.

In addition to observing dramatic thermomechanical improvements when Laponite was added to polyurethanes, fractal-like crystallites were observed under cross-polarized light to form upon annealing in only the Elasthane-based systems. It is not clear whether or not these crystallites influence the resultant thermomechanical properties. However, it is clear that at temperatures equal to or above 120°C and upon deformation the crystallite ordering is destroyed. But, if Laponite is present within the Elasthane-based system, the crystallites will re-form upon annealing at 60°C for more than two days. This may be the first instance in which ordering and crystallization behavior similar to that observed in thermotropic liquid crystalline polymers was observed in a polyurethane/clay nanocomposite.

Ultimately, characterization shows that the thermomechanical enhancement Laponite provides depends upon the polarity and hydrophilicity of the polyurethane soft segment. More work is needed to elucidate the mechanisms responsible for the resultant thermomechanical behavior.

7. Future Work

The results of the characterization of the polyurethane/Laponite nanocomposites have prompted one big question—what Laponite-induced mechanisms or interactions within the polyurethane are responsible for the dramatic thermomechanical enhancement? Although, numerous polymer/clay nanocomposites have been studied and multiple models predicting the resultant thermomechanical behavior developed, scientists still do not understand exactly how the nano-clay and polymer interact to produce such dramatic thermomechanical enhancement. By answering the following, smaller questions, I will gain insight and will be better able to answer the big question.

- How does Laponite move within the polyurethane during deformation?
- How does Laponite influence hydrogen and ionic bonding within the polyurethane?
- What is the influence of Laponite on the static mechanical behavior of the polyurethane at various temperatures?
- How do thermal treatments affect the mechanical behavior of the nanocomposite?

The answers to these four questions will add insight as to how nano-clays or other rigid nanoparticles strengthen, toughen, stiffen, and thermomechanically enhance other polymeric matrices. This would then help engineers and material scientists to systematically tailor the thermomechanical behavior of the polymeric nanocomposites they develop for specific applications.

The following sections contain a discussion of the work necessary in the future to answer the four smaller questions that may in turn elucidate how nano-clay dramatically enhances the thermomechanical material properties of polyurethane without hindering extensibility.

7.1 Laponite Movement during Deformation

By utilizing various characterization techniques, i.e. small angle x-ray scattering (SAXS), fourier transform infrared spectroscopy (FTIR), and cross-polarized microscopy in conjunction with various mechanical tests, the local orientational changes of Laponite within the thin film can be analyzed.

SAXS with in situ stretching allows the spacing between the Laponite platelets to be interrogated as the thin film is progressively deformed. Song et al have completed a similar study in which they found that within the elastic regime of the matrix material the d -spacing of the clay platelets varied in a reversible manner, increasing upon deformation but recovering to the original spacing upon removal of the imposed load [50]. Ultimately, the pairs of platelets with interspersed polymer acted as tiny nano-springs. It would be interesting to evaluate the Laponite d -spacing in Elasthane, because the characterization results discussed in Chapter 5.1-5 show that the nano-clay is preferentially embedded within the polyurethane hard domains. Quantifying the variation in the resultant platelet d -spacing with respect to macro-scale deformation would allow the movement and breakdown of the jammed Laponite structure to be connected to physical

mechanisms such as the breakdown of the hard domains, plastic yield, soft segment alignment, and strain-hardening.

Not only would SAXS and in situ stretching be useful, but FTIR and cross-polarized light microscopy in conjunction with in situ stretching could be used to correlate morphological changes in the jammed Laponite network with respect to the nanocomposite mechanical behavior. By monitoring the intensity of the IR signals associated with various bonds throughout the thin film using FTIR it would be possible to observe a bond signature, such as the free and hydrogen-bonded carbonyl bonds of the hard segment at 1733 cm^{-1} and 1712 cm^{-1} , respectively, which correspond to the Laponite association with the polyurethane hard domains [37, 95]. Subsequent observations monitoring how this bond signature changes with respect to deformation may also elucidate how the clay and/or hard segments move during deformation. Furthermore, capturing the birefringence of a thin-film nanocomposite during a tensile test may visually tie various types of deformation observed during uniaxial tensile testing, i.e. hard segment breakdown and Laponite jamming or soft segment alignment or strain hardening within the nanocomposite, to the disruption of the crystallite structures observed under cross-polarized shown in Figure 5.23.

In addition to the above mechanistic studies, analysis of the hysteretic behavior of the nanocomposites with various concentrations of Laponite is also imperative. If cyclic tensile tests of various nanocomposites are carried out to different final deformations, including values that exceed the critical strain which induces plastic yield or strain hardening, the influence of Laponite on the energy absorbing characteristics of the material can be captured. Specifically, from the hysteretic data the structural changes in the jammed network of Laponite can be inferred and the influence of Laponite on the stress-softening of the material can be deduced. Then adjustments can be made to a good thermoplastic polyurethane model, like that developed by Qi and Boyce, to account for the influence of dispersed, discotic nano-clay filler. It is important to develop models that accurately predict the mechanical behavior of polyurethanes when discotic particles are included so that engineers can use the model as a tool to aid in the design of energy absorbing structured materials.

Qi and Boyce have developed a constitutive model that predicts well the stress-strain behavior of thermoplastic polyurethanes by coupling the mechanical behavior to the evolution of the hard and soft domain morphology of the polyurethane matrix as strain increases [85]. The model captures the nonlinear hyperelastic behavior, time-dependence, stress-softening, and hysteretic behavior by virtue of a hyperelastic spring which acts in parallel to an elastic spring and viscoplastic dashpot that are placed in series. The model, constitutive equations, and parameters are shown below in Figure 7.1.

that adding Laponite, which is rigid and has a lateral dimension on the same scale as the lateral dimension of a hard domain, to the polyurethane was similar to adjusting the initial and final hard domain volume fraction. The soft domain fraction resultantly changes since the soft and hard domain fraction must at all times sum to one. When comparing the resultant changes in mechanical behavior due to these parameter adjustments to that of pure Elasthane and Elasthane filled with 10 and 20 wt% Laponite, as shown in Figures 7.3 and 7.4, it becomes obvious that these changes alone do not come close to predicting the actual behavior. As is shown if Figure 7.4 the addition of the rigid Laponite platelets to Elasthane dramatically changes the elastic modulus, permanent set, and hysteretic behavior of the polyurethane, all of which are properties that can be captured by the soft domain evolution (v_{so} , v_{ss}) and athermal shear strength (s) components of the model.

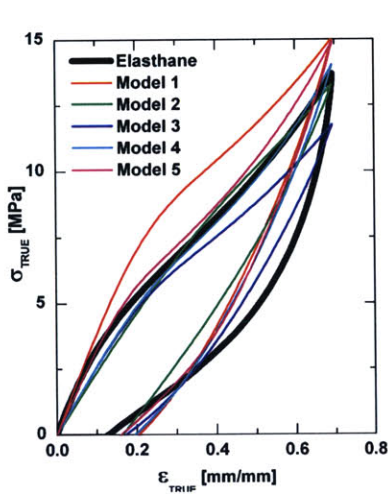


Figure 7. 3: Influence of adjustments in model parameters on stress-strain curve

Model	v_{SO}	v_{SS}	S_O MPa
1	0.5	0.9	2.4
2	0.7	0.9	2.4
3	0.7	0.9	1.4
4	0.7	0.8	1.4
5	0.6	0.8	1.4

Table 7. 2: Corresponding parameter values for the various models depicted in Figure 7.3

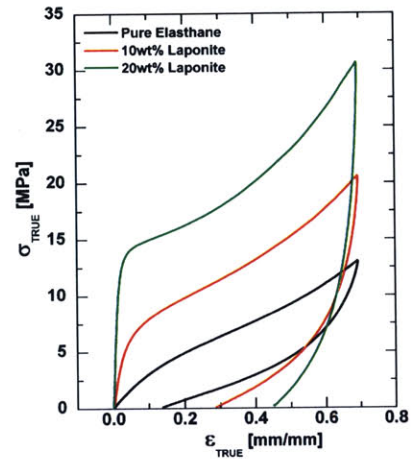


Figure 7. 4: Hysteretic behavior of pure Elasthane (black), 10 wt% (red) and 20 wt% (green) Laponite-filled Elasthane

After taking a closer look at the constitutive model of Qi and Boyce, it is clear that the amplification of the hyperelastic stress-response, X , is an extension of the Guth-Gold rigid particle filler model in which the hard domain volume fraction ($1-v_s$) is utilized as the rigid particle filler volume fraction. As was shown in Chapter 5.2, the Guth-Gold model fails when the volume fraction of Laponite is greater than the percolation limit. Consequently, changes in the effective soft domain volume fraction alone will not amplify the equilibrium stress-strain response enough when more than 6 wt% Laponite is added.

Ultimately, understanding the correspondence between deformation and structural changes, specifically the orientation of Laponite within the nanocomposites, may add insight as to how and to what extent the Laponite enhances the equilibrium stress-strain response of the polyurethane. This data can then be used to modify the constitutive model developed by Qi and Boyce to account for the affects of nano-clay reinforcement. Furthermore, if the movement and orientation of the Laponite is known the hard domain evolution can be deduced because Laponite and polyurethane hard domains are of similar size and Laponite preferentially reinforces the hard domains of Elasthane.

7.2 Influence of Laponite on Hydrogen and Ionic Bonding

From the dynamic mechanical analysis detailed in Chapter 5.3 it is clear that the heat distortion temperature of the Elasthane increases with increasing Laponite concentration. However, it is not clear whether this behavior is a consequence of Laponite jamming or enhancement of hard segment melting temperature. In general the melting temperature of a material is increased if the intermolecular cohesive bonds holding the material together are stronger [23]. Furthermore, the intensity of a hard segment melting endotherm increases when the crystallite is more pure and/or perfect [23]. Both of these characteristics are exhibited in the first heating cycle of DSC analysis when the Laponite concentration increases as shown in Figure 5.17. Consequently, Fourier transform infrared spectroscopy (FTIR) can be used to measure how the intensity of the free and hydrogen-bonded NH and C=O of the Elasthane varies with increasing Laponite concentration [37, 95]. If as the clay concentration increases the intensity of the peak at 1712 cm^{-1} , corresponding to the hydrogen-bonded carbonyl group of the urethane increases it can be concluded that the degree of hydrogen-bonding in Elasthane is increasing [95]. By evaluating the ratio of the intensities of the bonded and free peaks of the spectrum the origin of the enhancement in heat distortion temperature can be determined and the preferential association of the nano-clay with the hard domains of Elasthane can also be confirmed [95].

7.3 Influence of Laponite at Various Temperatures

As mentioned in the previous sub-section, Chapter 7.2, the physical mechanism resulting in enhancement of the heat distortion temperature of Elasthane with increasing Laponite concentration is not known. If the increase is a consequence of Laponite jamming, the mechanical behavior of the material at temperatures below and above the soft segment glass transition temperature via tensile tests will differ. At temperatures below the soft segment glass transition temperature when the mobility is limited, the increases in the stiffness of the nanocomposite will probably increase with power-law scaling with respect to the Laponite concentration, as occurred at room temperature for nanocomposites with Laponite concentrations above the percolation limit (Chapter 5.2). This is because the mechanical behavior of the nanocomposites will be dominated by the modulus of the glassy polymer [88]. However, at temperatures above the soft segment glass transition temperature the stiffness of the material will likely hinge upon the jamming and collision of Laponite platelets. If this behavior occurs as predicted then the increase in heat distortion temperature is in fact a result of the house-of-cards network formed at high Laponite concentrations. By evaluating the power-law scaling of the elastic moduli of nanocomposites containing various concentrations of Laponite at these high temperatures, the Laponite dispersal and resultant morphology may be further elucidated.

7.4 Influence of Thermal Treatments on Nanocomposite Mechanical Behavior

As is noted in Chapter 5.4, thermal processing history can dramatically modify the morphology and the resultant mechanical properties of polyurethanes [91, 92]. In the differential scanning calorimetry heat flow analysis of the Elasthane/Laponite nanocomposites presented in Figures 5.17 and 5.18 it was observed that after erasing the thermal processing history of the nanocomposite, by raising the sample temperature to 250°C , upon cooling at $10^{\circ}\text{C min}^{-1}$ the apparent hard segment crystallinity was destroyed. Furthermore, at high Laponite concentrations

not only was the hard segment crystallinity destroyed, but a new crystalline morphology became apparent.

It would be interesting to determine how the thermal treatments imposed on the sample via DSC affect the mechanical properties of the nanocomposite. By placing the thin films, after complete solvent removal in thermally conductive molds (e.g. metallic molds) and then using a thermoelectric (Peltier) heater/cooler it would be easy to thermally treat the thin films in a controlled manner. A thermoelectric heater/cooler affords good control over the maximum and minimum temperature as well as the heating/cooling rate to which the thin films would be subjected. Subsequently, after cooling and removal from the mold the annealed thin film could be mechanically tested as explained in Chapters 4.2.6 and 4.2.7 and the influence of the thermal treatment evaluated. Furthermore, after plastic deformation of the nanocomposite, it is worth investigating whether the energy lost (in terms of permanent plastic deformation), as shown in hysteretic data, can be recovered via heat treatment.

Shape memory polymers are those polymers that have a glass transition temperature above room temperature, have a sharp glass to rubber transition, and exhibit shape memory or entropically driven recovery [96, 97]. For example, a shape memory polymer is one that when deformed quickly at a temperature above its glass transition temperature (T_g) and then cooled to a temperature below T_g (while the load is still applied) will recover its original, un-deformed shape upon removal of the deforming load and heating to a temperature above T_g . A major application of shape memory polymers has been as heat shrink tubing, however, shape memory polymers offer great potential as actuators in numerous deployable applications [98]. Consequently, desirable shape memory polymers are those that exhibit both large stress and large strain recovery. Therefore, polyurethane/Laponite nanocomposites are excellent candidates since the addition of Laponite increases the rubbery plateau modulus significantly, as shown in Figure 5.11, which would in turn increase the stiffness and constrained recovery stress applied by the shape memory polyurethane/Laponite nanocomposite [98]. However, for polyurethane/Laponite nanocomposites to be successful as shape memory polymers the nanocomposite must be able to recover most, if not all, of its original shape after thermal treatment. Typically, as Mishra et al showed (Chapter 3), when particles, like Montmorillonite, are added to a polymer network some recoverable strain is lost because the clay disrupts the entanglement network [47, 98]. Laponite-based shape memory polymer nanocomposites may prove more efficient because Laponite is much smaller than Montmorillonite and may not interrupt the entanglement network as much, allowing strain recovery to be maximized.

It would also be interesting to determine how mechanical alignment in conjunction with heat treatment influences the mechanical behavior of the nanocomposites. By extending the polymer past its yield point to a point of good chain alignment and then heat treating the material, it may be possible to capture an aligned Laponite network rather than one that is jammed in a randomly oriented house-of-cards structure. It is not clear how the aligned network would modify the mechanical behavior of the nanocomposite. If alignment does not weaken the material, aligned Laponite nanocomposites could prove desirable in shape memory polymer applications because upon deformation the entanglement network may not be subjected to as great a disruption as when a house-of-cards network exists.

7.5 Summary

Thermoplastic polyurethane elastomer/Laponite nanocomposites are at their earliest stage in development. The findings reported in Chapter 5 show that these polyurethane/Laponite nanocomposites offer great potential as new, high-performance materials with good energy absorbency capabilities and great mechanical stability at high temperatures. Although it is not yet understood how Laponite induces these thermomechanical enhancements, it is important to evaluate these nanocomposites so that scientists can better tailor the nanostructure of synthetic materials to maximize energy absorbency and minimize heat distortion. Therefore, it is important to understanding how the structural orientation of Laponite within the polyurethane changes upon deformation and whether the increase in heat distortion temperature is a consequence of stronger intermolecular cohesive bonding or the house-of-cards network structure formed by the Laponite. Furthermore, by subjecting the nanocomposites to thermal and mechanical treatments the shape memory capabilities can be evaluated and further enhancement of the mechanical behavior may be achieved if the Laponite platelets are re-order or aligned. Ultimately, the nanostructure of these polyurethane/Laponite nanocomposites is ideal for further study; not only can the Laponite ordering be analyzed to better understand its influence on the thermomechanical behavior of the polyurethane, but the nanostructure can be further manipulated and new, thermomechanical behaviors induced.

References

- [1] F. Vollrath and D. P. Knight, "Liquid crystalline spinning of spider silk," *Nature*, vol. 410, pp. 541-548, 2001.
- [2] J. M. Gosline, P. A. Guerette, C. S. Ortlepp, and K. N. Savage, "The mechanical design of spider silks: From fibroin sequence to mechanical function," *Journal of Experimental Biology*, vol. 202, pp. 3295-3303, 1999.
- [3] C. Sutton, 2004, "Researchers Create Better Materials By Emulating Spider's Techniques," [Online], Retrieved April 24, 2005, from University California, Los Angeles Web site: <http://www.engineer.ucla.edu/stories/2002/spider.htm>.
- [4] A. Lazaris, S. Arcidiacono, Y. Huang, J. F. Zhou, F. Duguay, N. Chretien, E. A. Welsh, J. W. Soares, and C. N. Karatzas, "Spider silk fibers spun from soluble recombinant silk produced in mammalian cells," *Science*, vol. 295, pp. 472-476, 2002.
- [5] D. Porter, F. Vollrath, and Z. Z. Shao, "Predicting the mechanical properties of spider silk as a model nanostructured polymer," *The European Physical Journal E*, vol. 16, pp. 199-206, 2005.
- [6] MatWeb, 2005, "MatWeb Material Property Data," Automation Creations, Inc, [Online], Available: <http://matweb.com/index.asp?ckck=1>.
- [7] J. DeGaspari, April 2001, "Prospecting Paydirt," [Online], Retrieved February 17, 2005, from the Mechanical Engineering Magazine Web site: <http://www.memagazine.org/backissues/april01/features/prospect/prospect.html>.
- [8] P. C. LeBaron, Z. Wang, and T. J. Pinnavaia, "Polymer-layered silicate nanocomposites: an overview," *Applied Clay Science*, vol. 15, pp. 11-29, 1999.
- [9] S. S. Ray and M. Okamoto, "Polymer/layered silicate nanocomposites: a review from preparation to processing," *Progress in Polymer Science*, vol. 28, pp. 1539-1641, 2003.
- [10] N. Kumar, S. M. Liff, and G. H. McKinley, "Method to Disperse and Exfoliate Nanoparticles Within Polymer Matrices to Make High Polymer Performance Nanocomposites," U.S. Provisional Patent Application no. 0492611, Oct. 18, 2004.
- [11] Rockwood Specialties Inc., "Manufacture, structure and chemistry," [Online], Retrieved May 17, 2005 from Laponite Web site: <http://www.laponite.com/pdf/broch/science.pdf>.
- [12] D. P. Knight, M. M. Knight, and F. Vollrath, "Beta transition and stress-induced phase separation in the spinning of spider dragline silk," *International Journal of Biological Macromolecules*, vol. 27, pp. 205-210, 2000.
- [13] M. Xu and R. V. Lewis, "Structure of a Protein Superfiber - Spider Dragline Silk," *Proceedings of the National Academy of Sciences of the United States of America*, vol. 87, pp. 7120-7124, 1990.
- [14] D. T. Grubb and L. W. Jelinski, "Fiber morphology of spider silk: The effects of tensile deformation," *Macromolecules*, vol. 30, pp. 2860-2867, 1997.
- [15] L. W. Jelinski, "Establishing the relationship between structure and mechanical function in silks," *Current Opinion in Solid State & Materials Science*, vol. 3, pp. 237-245, 1998.
- [16] C. Y. Hayashi, N. H. Shipley, and R. V. Lewis, "Hypotheses that correlate the sequence, structure, and mechanical properties of spider silk proteins," *International Journal of Biological Macromolecules*, vol. 24, pp. 271-275, 1999.
- [17] J. P. O'Brien, S. R. Fahnestock, Y. Termonia, and K. C. H. Gardner, "Nylons from nature: Synthetic analogs to spider silk," *Advanced Materials*, vol. 10, pp. 1185+, 1998.

- [18] Y. Yang, X. Chen, Z. Z. Shao, P. Zhou, D. Porter, D. P. Knight, and F. Vollrath, "Toughness of spider silk at high and low temperatures," *Advanced Materials*, vol. 17, pp. 84-88, 2005.
- [19] D. Randall and S. Lee, Ed., *The Polyurethanes Book*, 2nd ed., New York: Huntsman International, 2002.
- [20] T. Thomson, *Polyurethanes as Specialty Chemicals: Principles and Applications*. Boca Raton, Florida: CRC Press, 2005.
- [21] M. Michalovic, 1995, "The Macrogalleria: A Cyberwonderland of Polymer Fun," [Online], Retrieved April 5, 2004 from the University of Southern Mississippi Web site: <http://www.pslc.ws/mactest/index.htm>.
- [22] M. Szycher, *Szycher's Handbook of Polyurethanes*. Boca Raton, Florida: CRC Press, 1999.
- [23] R. J. Young and P. A. Lovell, *Introduction to Polymers*. Cheltenham, U.K.: Nelson Thornes Ltd., 1991.
- [24] M. Song, H. S. Xia, K. J. Yao, and D. J. Hourston, "A study on phase morphology and surface properties of polyurethane/organoclay nanocomposite," *European Polymer Journal*, vol. 41, pp. 259-266, 2005.
- [25] K. Yano, A. Usuki, and A. Okada, "Synthesis and Properties of Polyimide-Clay Hybrid Films," *Journal of Polymer Science Part A-Polymer Chemistry*, vol. 35, pp. 2289-2294, 1997.
- [26] T. Lan and T. J. Pinnavaia, "Clay-Reinforced Epoxy Nanocomposites," *Chemistry Of Materials*, vol. 6, pp. 2216-2219, 1994.
- [27] E. P. Giannelis, "Polymer layered silicate nanocomposites," *Advanced Materials*, vol. 8, pp. 29-35, 1996.
- [28] C. M. Koo, H. T. Ham, S. O. Kim, K. H. Wang, I. J. Chung, D. C. Kim, and W. C. Zin, "Morphology evolution and anisotropic phase formation of the maleated polyethylene-layered silicate nanocomposites," *Macromolecules*, vol. 35, pp. 5116-5122, 2002.
- [29] Rockwood Specialties Inc., "Nanoclay.com," [Online], Retrieved May 17, 2005 from the Nanoclay Web site: <http://www.nanoclay.com>.
- [30] Y. Termonia, "Molecular Modeling of Spider Silk Elasticity," *Macromolecules*, vol. 27, pp. 7378-7381, 1994.
- [31] T. B. Murphy and A. F. Sawyer, 2004, "Advancement of natural and synthetic clays in personal care applications," [Online], Retrieved May 9, 2005 from the Global Cosmetics Manufacturing Web site: bbriefings.com/pdf/846/SudChemie_Tech.pdf.
- [32] Z. Wang and T. Pinnavaia, "Nanolayer Reinforcement of Elastomeric Polyurethane," *Chemistry of Materials*, vol. 10, pp. 3769-3771, 1998.
- [33] K. J. Yao, M. Song, D. J. Hourston, and D. Z. Luo, "Polymer/layered clay nanocomposites: 2 polyurethane nanocomposites," *Polymer*, vol. 43, pp. 1017-1020, 2002.
- [34] T. K. Chen, Y. I. Tien, and K. H. Wei, "Synthesis and characterization of novel segmented polyurethane clay nanocomposite via poly(epsilon-caprolactone)/clay," *Journal of Polymer Science Part a-Polymer Chemistry*, vol. 37, pp. 2225-2233, 1999.
- [35] S. Y. Moon, J. K. Kim, C. Nah, and Y. S. Lee, "Polyurethane/montmorillonite nanocomposites prepared from crystalline polyols, using 1,4-butanediol and organoclay hybrid as chain extenders," *European Polymer Journal*, vol. 40, pp. 1615-1621, 2004.

- [36] T. K. Chen, Y. I. Tien, and K. H. Wei, "Synthesis and characterization of novel segmented polyurethane/clay nanocomposites," *Polymer*, vol. 41, pp. 1345-1353, 2000.
- [37] Y. I. Tien and K. H. Wei, "Hydrogen bonding and mechanical properties in segmented montmorillonite/polyurethane nanocomposites of different hard segment ratios," *Polymer*, vol. 42, pp. 3213-3221, 2001.
- [38] Y. I. Tien and K. H. Wei, "High-Tensile-Property Layered Silicates/Polyurethane Nanocomposites by Using Reactive Silicates as Pseudo Chain Extenders," *Macromolecules*, vol. 34, pp. 9045-9052, 2001.
- [39] Y. I. Tien and K. H. Wei, "The Effect of Nano-Sized Silicate Layers from Montmorillonite on Glass Transition, Dynamic Mechanical and Thermal Degradation Properties of Segmented Polyurethane," *Journal of Applied Polymer Science*, vol. 86, pp. 1741-1748, 2002.
- [40] R. Xu, M. Evangelos, A. J. Snyder, and J. Runt, "New Biomedical Poly(urethane urea)--Layered Silicate Nanocomposites," *Macromolecules*, vol. 34, pp. 337-339, 2001.
- [41] R. J. Xu, E. Manias, A. J. Snyder, and J. Runt, "Low permeability biomedical polyurethane nanocomposites," *Journal Of Biomedical Materials Research Part A*, vol. 64A, pp. 114-119, 2003.
- [42] M. Tortora, G. Gorrasi, V. Vittoria, G. Galli, S. Ritrovati, and E. Chiellini, "Structural characterization and transport properties of organically modified montmorillonite/polyurethane nanocomposites," *Polymer*, vol. 43, pp. 6147-6157, 2002.
- [43] M. A. Osman, V. Mittal, M. Morbidelli, and U. W. Suter, "Polyurethane adhesive nanocomposites as gas permeation barrier," *Macromolecules*, vol. 36, pp. 9851-9858, 2003.
- [44] X. J. Wang, J. J. Kang, Y. P. Wu, and S. B. Fang, "Novel composite polymer electrolytes based on poly(ether-urethane) network polymer and modified montmorillonite," *Electrochemistry Communications*, vol. 5, pp. 1025-1029, 2003.
- [45] Y. W. Chen-Yang, H. C. Yang, G. J. Li, and Y. K. Li, "Thermal and anticorrosive properties of polyurethane/clay nanocomposites," *Journal Of Polymer Research*, vol. 11, pp. 275-283, 2004.
- [46] B. Finnigan, D. Martin, P. Halley, R. Truss, and K. Campbell, "Morphology and properties of thermoplastic polyurethane nanocomposites incorporating hydrophilic layered silicates," *Polymer*, vol. 45, pp. 2249-2260, 2004.
- [47] J. K. Mishra, I. Kim, and C. S. Ha, "Heat shrinkable behavior and mechanical response of a low-density polyethylene/millable polyurethane/organoclay ternary nanocomposite," *Macromolecular Rapid Communications*, vol. 25, pp. 1851-1855, 2004.
- [48] I. Rhoney, S. Brown, N. E. Hudson, and R. A. Pethrick, "Influence of processing method on the exfoliation process for organically modified clay systems. I. Polyurethanes," *Journal of Applied Polymer Science*, vol. 91, pp. 1335-1343, 2004.
- [49] R. Krishnamoorti and R. A. Vaia, Ed., *Polymer Nanocomposites: Synthesis, Characterization, and Modeling*, 1st ed., Washington, D.C.: Oxford University Press, 2002.
- [50] M. Song and K. J. Yao, "X-ray diffraction detection of compliance in polyurethane-organoclay nanocomposites," *Materials Science And Technology*, vol. 20, pp. 989-992, 2004.
- [51] K. C. Khemani, Ed., *Polymeric Foams: Science and Technology*, 1st ed., Washington, D.C.: American Chemical Society, 1997.

- [52] X. Cao, L. J. Lee, T. Widya, and C. Macosko, "Polyurethane/clay nanocomposites foams: processing, structure and properties," *Polymer*, vol. 46, pp. 775-783, 2005.
- [53] L. Song, Y. Hu, Y. Tang, R. Zhang, Z. Y. Chen, and W. C. Fan, "Study on the properties of flame retardant polyurethane/organoclay nanocomposite," *Polymer Degradation And Stability*, vol. 87, pp. 111-116, 2005.
- [54] N. Sheng, M. C. Boyce, D. M. Parks, G. C. Rutledge, J. I. Abes, and R. E. Cohen, "Multiscale micromechanical modeling of polymer/clay nanocomposites and the effective clay particle," *Polymer*, vol. 45, pp. 487-506, 2004.
- [55] D. Barthelmy, 2004, "Mineralogy Database," [Online], Available: <http://webmineral.com/>.
- [56] X. Y. Ma, H. J. Lu, G. Z. Liang, and H. X. Yan, "Rectorite/thermoplastic polyurethane nanocomposites: Preparation, characterization, and properties," *Journal Of Applied Polymer Science*, vol. 93, pp. 608-614, 2004.
- [57] C. Zilg, F. Dietsche, B. Hoffmann, C. Dietrich, and R. Mulhaupt, "Nanofillers based upon organophilic layered silicates," *Macromolecular Symposia*, vol. 169, pp. 65-77, 2001.
- [58] C. Zilg, R. Thomann, R. Mulhaupt, and J. Finter, "Polyurethane nanocomposites containing laminated anisotropic nanoparticles derived from organophilic layered silicates," *Advanced Materials*, vol. 11, pp. 49-52, 1999.
- [59] S. Varghese, K. G. Gatos, A. A. Apostolov, and J. Karger-Kocsis, "Morphology and mechanical properties of layered silicate reinforced natural and polyurethane rubber blends produced by latex compounding," *Journal Of Applied Polymer Science*, vol. 92, pp. 543-551, 2004.
- [60] H. C. Kuan, W. P. Chuang, and C. C. M. Ma, "Synthesis and characterization of a clay/waterborne polyurethane nanocomposite," *Journal Of Materials Science*, vol. 40, pp. 179-185, 2005.
- [61] Rockwood Specialties Inc., "Formulating with Laponite," [Online], Retrieved May 17, 2005 from Laponite Web site: <http://www.laponite.com/pdf/broch/formulation.pdf>.
- [62] Polymer Technology Group, 2002, "Elasthane Polyetherurethane," [Online], Retrieved April 5, 2004 from the Polymer Technology Group Web site: <http://www.polymertech.com/materials/elasthane.html>.
- [63] M. J. Wiggins, M. MacEwan, J. M. Anderson, and A. Hiltner, "Effect of soft-segment chemistry on polyurethane biostability during in vitro fatigue loading," *Journal of Biomedical Materials Research*, vol. 68A, pp. 668-683, 2004.
- [64] E. M. Christenson, M. Dadsetan, M. Wiggins, J. M. Anderson, and A. Hiltner, "Poly(carbonate urethane) and poly(ether urethane) biodegradation: In vivo studies," *Journal of Biomedical Materials Research*, vol. 69A, pp. 407-416, 2004.
- [65] L. James-Korley, "PEO-containing Copolymers as Polyurethane Soft Segments in the Development of High Performance Materials," Doctoral thesis, Massachusetts Institute of Technology, 2005.
- [66] G. Pollock, "Synthesis and Characterization of Mechanically Enhanced, Nanostructured Thermoplastic Polyurethane Elastomers," Doctoral thesis, Massachusetts Institute of Technology, 2005.
- [67] C. L. Yaws, X. Lin, L. Bu, D. R. Balundgi, and S. Tripathi, "Vapor Pressure," in *Chemical Properties Handbook*, C. L. Yaws, Ed. New York: McGraw-Hill, 1999, pp. 784.

- [68] A. Carli, S. Di Cave, and E. Sebastiani, "Thermodynamic characterization of vapour-liquid equilibria of mixtures acetic acid--dimethylacetamide and water--dimethylacetamide," *Chemical Engineering Science*, vol. 27, pp. 993-1001, 1972.
- [69] H. S. Lee and S. L. Hsu, "An Analysis of Phase Separation Kinetics of Model Polyurethanes," *Macromolecules*, vol. 22, pp. 1100-1105, 1989.
- [70] D. Chescoe and P. J. Goodhew, *The Operation of Transmission and Scanning Electron Microscopes*. New York, NY: Oxford University Press, 1990.
- [71] W. W. Scott and B. Bhushan, "Use of phase imaging in atomic force microscopy for measurement of viscoelastic contrast in polymer nanocomposites and molecularly thick lubricant films," *Ultramicroscopy*, vol. 97, pp. 151-169, 2003.
- [72] R. Howland and L. Benatar, *A Practical Guide to Scanning Probe Microscopy*. Sunnyvale, CA: ThermoMicroscopes, Inc., 2000.
- [73] Scintag Inc., 1999, "Chapter 7: Basics of X-Ray Diffraction," [Online], Retrieved March 20, 2005 from the University of New Mexico Web site: <http://epswww.unm.edu/xrd/resources.htm>.
- [74] D. Campbell, R. A. Pethrick, and J. R. White, *Polymer Characterization: Physical Techniques*, 2nd ed. Cheltenham, U.K.: Stanley Thornes, 2000.
- [75] TA Instruments Inc., 1997, "Modulated DSCTM Compendium: Basic Theory and Experimental Considerations, TA-210," [Online], Retrieved August 17, 2004 from the TA Instruments, Inc. Web site: <http://tainstruments.com/main.asp?n=2&id=147>.
- [76] TA Instruments Inc., 1999, "Modulated DSC (MDSC): How Does it Work?" [Online], Retrieved August 17, 2004 from the TA Instruments, Inc. Web site: <http://tainstruments.com/main.asp?n=2&id=147>.
- [77] TA Instruments Inc., 2002, "TA Instruments Dynamic Mechanical Analyzer," [Online], Retrieved March 5, 2005 from the TA Instruments, Inc. Web site: <http://tainstruments.com/main.asp?n=2&id=147>.
- [78] D. W. van Krevelen, *Properties of Polymers: Their Correlation with Chemical Structure; Their Numerical Estimation and Prediction From Additive Group Contributions*, 3rd ed. Amsterdam, NL: Elsevier Science, 1997.
- [79] TA Instruments Inc., 1999, "Dynamic Mechanical Analyzers: How Do They Work?" [Online], Retrieved March 5, 2005 from the TA Instruments, Inc. Web site: <http://tainstruments.com/main.asp?n=2&id=147>.
- [80] N. E. Dowling, *Mechanical Behavior of Materials*, 2nd ed. Upper Saddle River, NJ: Prentice Hall, Inc, 1999.
- [81] P. C. Robinson and M. W. Davidson, 2005, "Nikon MicroscopyU: Polarized Light Microscopy," [Online], Retrieved March 16, 2005 from the Nikon MicroscopyU Web site: <http://www.microscopyu.com/articles/polarized/polarizedintro.html>.
- [82] S. Hirokawa, K. Yamamoto, and T. Kawada, "A Photoelastic Study of Ligament Strain," *IEEE Transactions on Rehabilitation Engineering*, vol. 6, pp. 300-308, 1998.
- [83] D. J. Martin, G. F. Meijs, G. M. Renwick, S. J. McCarthy, and P. A. Gunatillake, "The effect of average soft segment length on morphology and properties of a series of polyurethane elastomers.1. Characterization of the series," *Journal of Applied Polymer Science*, vol. 62, pp. 1377-1386, 1996.
- [84] M. Niesten and R. J. Gaymans, "Tensile and elastic properties of segmented copolyetheresteramides with uniform aramid units," *Polymer*, vol. 42, pp. 6199-6207, 2001.

- [85] H. J. Qi and M. C. Boyce, "Stress-strain behavior of thermoplastic polyurethanes," *Mechanics of Materials*, vol. 37, pp. 817-839, 2005.
- [86] J. Krijgsman and R. J. Gaymans, "Tensile and elastic properties of thermoplastic elastomers based on PTMO and tetra-amide units," *Polymer*, vol. 45, pp. 437-446, 2004.
- [87] E. Guth, "Theory of Filler Reinforcement," *Journal of Applied Physics*, vol. 16, pp. 20-25, 1945.
- [88] C. S. O'Hern, L. E. Silbert, A. J. Liu, and S. R. Nagel, "Jamming at zero temperature and zero applied stress: The epitome of disorder," *Physical Review E*, vol. 68, pp. 011306, 2003.
- [89] L. E. Nielsen and R. F. Landel, *Mechanical Properties of Polymers and Composites*, 2nd ed. New York: Marcel Dekker, Inc., 1994.
- [90] T. K. Chen, T. S. Shieh, and J. Y. Chui, "Studies on the First DSC Endotherm of Polyurethane Hard Segment Based on 4,4'-Diphenylmethane Diisocyanated and 1,4-Butanediol," *Macromolecules*, vol. 31, pp. 1312-1320, 1998.
- [91] D. J. Martin, G. F. Meijs, P. A. Gunatillake, S. J. McCarthy, and G. M. Renwick, "The effect of average soft segment length on morphology and properties of a series of polyurethane elastomers.2. SAXS-DSC annealing study," *Journal of Applied Polymer Science*, vol. 64, pp. 803-817, 1997.
- [92] R. W. Seymour and S. L. Cooper, "Thermal Analysis of Polyurethane Block Polymers," *Macromolecules*, vol. 6, pp. 48-53, 1973.
- [93] A. Saiani, W. A. Daunch, H. Verbeke, J. W. Leenslag, and J. S. Higgins, "Origin of Multiple Melting Endotherms in a High Hard Block Content Polyurethane. 1. Thermodynamic Investigation," *Macromolecules*, vol. 34, pp. 9059-9068, 2001.
- [94] A. Aneja and G. L. Wilkes, "A systematic series of 'model' PTMO based segmented polyurethanes reinvestigated using atomic force microscopy," *Polymer*, vol. 44, pp. 7221-7228, 2003.
- [95] X. H. Dai, J. Xu, X. L. Guo, Y. L. Lu, D. Y. Shen, N. Zhao, X. D. Luo, and X. L. Zhang, "Study on structure and orientation action of polyurethane nanocomposites," *Macromolecules*, vol. 37, pp. 5615-5623, 2004.
- [96] E. R. Abrahamson, M. S. Lake, N. A. Munshi, and K. Gall, "Shape Memory Mechanics of an Elastic Memory Composite Resin," *Journal of Intelligent Material Systems and Structures*, vol. 14, pp. 623-632, 2003.
- [97] Y. Liu, K. Gall, M. L. Dunn, and P. McCluskey, "Thermomechanics of shape memory polymer nanocomposites," *Mechanics of Materials*, vol. 36, pp. 929-940, 2004.
- [98] K. Gall, M. L. Dunn, Y. Liu, D. Balzar, and G. Stefanic, "Internal Stress Storage in Shape Memory Polymer Nanocomposites," *Applied Physics Letters*, vol. 85, pp. 290-292, 2004.

Author	Journal	Date	Polyurethane	Filler	Dispersal Method	Samples	Dispersal	Mechanical Findings	Thermal Findings	Barrier Properties	Notes
Song, L., Hu, Y., Tang, Y., Zhang, R., Chen, Z., & Fan, W.	Polymer Degradation and Stability	2005	Toluene diisocyanate and poly(propylene oxide) glycol M=1000, 8 diglycol chain extender and glycerine crosslinking agent in DMF	Sodium Montmorillonite with hexadecyl-trimethyl ammonium chloride and triamine polyphosphate(5wt% OMT, 6wt% MPP, 3 5wt% OMT+6wt% MPP)	in situ polymerization (clay 1st dispersed in polyether)	cured at 100°C	XRD and TEM show intercalation with gallery spacing between 4 and 5nm (increased from 1.3nm MMT and 2.1 nm OMT)	Tensile strength increases with filler. PU=1.53MPa, PU/OMT=2.91MPa, PU/MPP=2.11 MPa, PU/OMT/MPP=3.59MPa. Note: MPP can hydrogen bond with TDI.	The rate of weight loss with respect to increasing temperature decreases with increased filler content. The heat release rate, mass loss rate, specific extinction area, CO release amount and CO2 release amount all decrease significantly when MPP and OMT are added to the PU. Ultimately the flame retardance increases with filler.	NA	The lower flammability of the PU/clay/MPP composite occurs because a carbonaceous-silicious-phosphorated char layers coat and protect the polymer interior.
Song, M., Xia, H.S., Yao, K.J., & Hourston, D.J.	European Polymer Journal	2005	Polypropylene glycol (Lupanol 2090 M=6000), 4,4'-Methylene bis(cyclohexyl isocyanate), 1,4-butanediol, Dabco-33LV, 8 Stannous 2-ethyl hexanoate 18, 26, 36wt% hard segment	Closte 20A which is modified with dihydrogenated tallow, quaternary ammonium @ 1, 3, 85wt%	in situ polymerization (clay dispersed in polyol 1st)	cured @ 50°C for 24 hrs & 80°C for a week	SAXS data was analyzed assuming isotropically distributed stack of alternating crystalline and amorphous lamellae. The inter-domain repeat distance increased with hard segment content (57nm, 84 nm, 89nm--18%,26%,36%) but decreased with clay content (15%, 7.1%, 8.3 4% respectively @5wt% loading). The hard domains were 12-32nm in size and increased with hard segment content and decreased slightly with the addition of clay. This behavior can be explained by the affect of clay on soft segment behavior--more clay causes the polyol chains to be more tightly coiled.	Mean adhesion force of AFM tip decreased with the addition of organoclay, indicating the surface energy decreased. This was an effect due to the organic modifier.	NA	NA	AFM showed hard domain spherical aggregates (~800nm pure and ~500nm with clay)

Appendix B: ABAQUS Input File

tension_test_sml.inp

```
*HEADING
one 4-node cont ele
*NODE
1, 0., 0., 0.
2, 1., 0., 0.
3, 1., 1., 0.
4, 0., 1., 0.
*ELEMENT, TYPE=CPE4H, ELSET=ALL
1, 1,2,3,4
*SOLID SECTION,ELSET=ALL,MATERIAL=pu
*NSET, nset=top
4
*NSET, nset=bottom
2, 1
*NSET, nset=left
1, 4
*NSET, nset=all
1,2,3,4
***PU material
*material,name=pu
*USER MATERIAL,CONSTANTS=10
38.0D6,0.48D0,1.34D-2,1.64D-20,1.39D6,1.40D6,6.0D0,0.6
0.800,1.4
*DEPVAR
17
*user output variables
15
*INITIAL CONDITIONS, TYPE=TEMPERATURE
ALL,300.
*material,name=ep
*elastic
2.e11,0.3
*plastic
250e6
*EQUATION
2
2,1,1.,3,1,-1.
2
3,2,1.,4,2,-1.
**
** Step 1: loading
```

```

**
*STEP,name=Step-1,INC=10000,NLGEOM
*STATIC
0.05,60,1E-7,0.5
*BOUNDARY
top, 2, 2, 1.
bottom, 2, 2
left, 1, 1
*End Step
*STEP,name=Step-2,INC=10000,NLGEOM
*STATIC
0.05,60,1E-5,0.5
*BOUNDARY ,op=new
top, 2, 2, 0.
bottom, 2, 2
left, 1,1
**RESTART, WRITE, FREQ=0
*END STEP
*STEP,name=Step-3,INC=10000,NLGEOM
*STATIC
0.05,60,1E-5,0.5
*BOUNDARY ,op=new
top, 2, 2, 1.
bottom, 2, 2
left, 1,1
**RESTART, WRITE, FREQ=0
*END STEP
*STEP,name=Step-4,INC=10000,NLGEOM
*STATIC
0.05,60,1E-5,0.5
*BOUNDARY ,op=new
top, 2, 2, 0.
bottom, 2, 2
left, 1,1
**RESTART, WRITE, FREQ=0
*END STEP

```

Appendix C: ABAQUS Subroutine File

pu_sml.disp

```
      SUBROUTINE DISP (U,KSTEP,KINC,TIME,NODE,NOEL,JDOF,COORDS)
C
C      INCLUDE 'ABA_PARAM.INC'
C
C      DIMENSION U(3),TIME(2),COORDS(3)
C      COMMON /KFLAG/ T1,T2,IFLAG
C
C      IF(TIME(2).LT.1.D-10) IFLAG=0
C
C      UDOT=1.D0/60.D0
C      UTILDE = 1.D0
C      T1=UTILDE/UDOT*1.001D0
c      write(6,*) time(2),T2,IFLAG
C
C      IF (TIME(2).LT.T1) THEN
C      U(1) = UDOT*TIME(2)
C      write(6,*) time(2),'A'
C      ELSE IF (TIME(2).GE.T1.AND.IFLAG.EQ.0) THEN
C      write(6,*) time(2),'B'
C      U(1) = 2.D0*UTILDE-UDOT*TIME(2)
C      ELSE
c      write(6,*) time(2),'C'
C      U(1) = UDOT*TIME(2)+2.D0*(UTILDE-UDOT*T2)
C
C      END IF
c      write(6,*) u(1),time(2),t2
C
C      RETURN
C      END
C
C      SUBROUTINE UVARM (UVAR,DIRECT,T,TIME,DTIME,CMNAME,ORNAME,
1  NUVARM,NOEL,NPT,LAYER,KSPT,KSTEP,KINC,NDI,NSHR,COORD,
2  JMAC,JMATYP,MATLAYO,LACCFLA)
C
C      INCLUDE 'ABA_PARAM.INC'
C
C      CHARACTER*80 CMNAME
C      CHARACTER*80 ORNAME
C      CHARACTER*3 FLGRAY(15)
```

```

    DIMENSION UVAR(NUVARM),DIRECT(3,3),T(3,3),TIME(2)
    DIMENSION ARRAY(15),JARRAY(15),JMAC(*),JMATYP(*),COORD(*)
COMMON /KFLAG/ T1,T2,IFLAG

```

```

SIGTOL=1.D2

```

C

```

IF(TIME(2).LT.1.D-10) IFLAG=0

```

```

    UVAR(1)=0.D0 ! Just a dummy output

```

```

    CALL GETVRM ('S',ARRAY,JARRAY,FLGRAY,JRCD,JMAC,JMATYP,MATLAYO,
1  LACCFLA)

```

```

c    write(6,*) 'STRESS33=',ARRAY(3),time(2)
c    IF(IFLAG.EQ.0.AND.ARRAY(3).LT.SIGTOL.AND.TIME(2).GT.T1)THEN
c        IFLAG=1
c        T2=TIME(2)
c    END IF

```

```

IF (KSTEP.EQ.2.AND.ARRAY(2).LT.SIGTOL) THEN

```

```

UTILDE=1.0D0

```

```

    UDOT=1.D0/60.D0

```

```

    WRITE(6,*) 'DISP: ',2.D0*UTILDE-UDOT*TIME(2)

```

```

WRITE(6,*) 'TOTAL TIME: ',TIME(2)

```

```

    T2=TIME(2)

```

```

    WRITE(6,*) 'STEP TIME: ',TIME(1)

```

```

WRITE(6,*) 'STEP: ',KSTEP

```

```

c    CALL XIT

```

```

    END IF

```

```

IF (KSTEP.EQ.4.AND.ARRAY(2).LT.SIGTOL) THEN

```

```

UTILDE=1.D0

```

```

    UDOT=1.D0/60.D0

```

```

    WRITE(6,*) 'DISP: ',4.D0*UTILDE-UDOT*TIME(2)

```

```

WRITE(6,*) 'TOTAL TIME: ',TIME(2)

```

```

    WRITE(6,*) 'STEP TIME: ',TIME(1)

```

```

WRITE(6,*) 'STEP: ',KSTEP

```

```

c    CALL XIT

```

```

    END IF

```

```

    RETURN

```

```

    END

```